# Optimal ash particle refractive index model for simulating the brightness temperature spectrum of volcanic ash clouds from satellite infrared sounder measurements

Hiroshi Ishimoto[1], Masahiro Hayashi[1], Yuzo Mano[1]

5  [1]Meteorological Research Institute, Tsukuba, 305-0052, Japan

*Correspondence to*: Hiroshi Ishimoto (hiroishi@mri-jma.go.jp)

**Abstract.** Using data from the Infrared Atmospheric Sounding Interferometer (IASI) measurements of volcanic ash clouds and radiative transfer calculations, we identify the optimal refractive index model for simulating the measured brightness temperature spectrum of volcanic ash material. We assume that the optimal refractive index model has the smallest root mean

10  square of the brightness temperature difference between measurements and simulations for channels in the wavenumber range of 750–1400 cm$^{-1}$ and compare 21 refractive index models for optical properties of ash particles, including recently published models. From the results of numerical simulations for 164 pixels of IASI measurements for ash clouds from 11 volcanoes, we found that the measured brightness temperature spectrum could be well simulated using certain newly established refractive index models. In the cases of Eyjafjallajökull and Grímsvötn ash clouds, the optimal refractive index models determined

15  through numerical simulation correspond to those deduced from the chemical composition of ash samples for the same volcanic eruption events. This finding suggests that infrared sounder measurement of volcanic ash clouds is an effective approach to estimating the optimal refractive index model. However, discrepancies between the estimated refractive index models based on satellite measurements and the associated volcanic rock types were observed for some volcanic events.

## 1. Introduction

20  For continuous near-real time monitoring of volcanic ash clouds (VACs) during both day and night, satellite observations obtained using infrared sensors are particularly useful (Mackie and Watson, 2014; Mackie et al., 2016; Clarisse and Prata, 2016). Because volcanic silicate has a characteristic absorption band around 10 μm due to the stretching vibration of the Si-O bond, VACs containing fine ash particles can be easily detected and distinguished from water or ice clouds through measurement of the brightness temperature difference between two channels in this absorption band, such as 10.8 μm and

25  12 μm (Wen and Rose, 1994; Prata and Grant, 2001). Applying further constraints related to the atmospheric profile and microphysical properties of the ash particles, such as the particle size distribution, the physical properties of VACs (cloud height, particle effective radius, optical depth, and the associated ash mass loading) were determined using measurements in other infrared channels from high-resolution satellite imagers (Francis et al., 2012; Pavolonis et al., 2013, 2015a, 2015b; Prata and Lynch, 2019) and satellite infrared sounders (Clarisse et al., 2010, 2013; Ventress et al., 2016; Clarisse and Prata, 2016).

30  These retrieval methods are based on the results of radiative transfer calculations for the measured infrared brightness temperature of VACs under assumed atmospheric profiles and surface conditions, therefore the optical properties of the ash particles are essential. In particular, the complex refractive index (RI) is an important upstream parameter for estimation of ash optical properties and their wavelength dependence.

A typical RI model over a wide range of infrared wavelengths, the "andesite" model proposed by Pollack et al. (1973)

35  (hereinafter PL1973) has been adopted for radiative transfer calculations for volcanic ash analysis. Although the andesite model of PL1973 provides suitable approximations for analysis of some VACs (Pavolonis et al., 2013), simulations of the infrared brightness temperature spectrum (BTS) of VACs based on radiative transfer calculations from PL1973 andesite often caused large discrepancies relative to calculations based on satellite infrared sounder measurements (Gangale et al., 2010;

Newman et al., 2012; Ishimoto et al., 2016; Clarisse and Prata, 2016). For simulation of a measured BTS to retrieve the physical

40 properties of a VAC from satellite data, RI models that account for variations in the chemical composition of volcanic ash are essential. Optical properties of ash particles calculated using the optimal RI model for the observed VAC support accurate and robust determination of the physical properties of VACs in satellite image analysis. Furthermore, a good RI model leads to improvements in existing retrieval algorithms—no only for ash particles but also for volcanic SO₂ gas levels—through accurate estimation of the contribution of ash to the measured brightness temperature.

45 In recent years, two RI datasets for volcanic ash material over broad infrared wavelength regions have been proposed. One dataset is built from the results of laboratory experiments using ash sampled from several volcanoes (Reed et al., 2017, 2018). Based on the results of Reed et al. (2018), Prata et al. (2019) provided another RI dataset that is parameterised using $SiO_2$ content or the ratio of non-bridging oxygens to tetrahedrally coordinated cations (NBO/T). If an appropriate RI model for analysis of the measured VAC from satellite data is provided by the RI dataset of Reed et al. (2018), the RI model can be

50 estimated based on similarity with the rock type of the target volcano. Furthermore, if the $SiO_2$ content and/or NBO/T parameterisations of Prata et al. (2019) are effective, we can identify the optimal RI model, for example, from the chemical composition of ash or pumice samples from on-going or past eruption events. However, whether the selected RI model accurately reproduces satellite measurements via radiative transfer calculations remains unclear.

The most appropriate satellite measurement type to discuss such reproducibility is a BTS obtained using an infrared sounder.

55 In this work, we attempt to identify the most appropriate RI model from recently proposed RI datasets by comparing BTSs between satellite measurements and numerical simulations without compositional constraints for the ash material. If the RI model obtained from infrared sounder measurements corresponds to that derived from $SiO_2$ content or NBO/T for a sample from the same volcano, the results are considered to support the validity of the RI model based on ash chemical composition. Volcanic ash particles in the atmosphere may have differing optical properties compared to sampled ash particles due to

60 modification in the atmosphere, such as condensation of ice, water, or sulphate on ash particles. Even pure ash particles identified from satellite infrared observations may have differing compositions from ash or pumice samples (Carn and Krotkov, 2016). The particle sizes of ash clouds, which can be determined from the negative brightness temperature difference between two infrared split-window channels, are generally small (Clarisse and Prata, 2016), with estimated effective radii generally less than 5 μm. For such fine ash particles, silicic micropumice and small glass shards may remain in the atmosphere longer

65 than particles of the bulk composition due to their density (Cashman and Rust, 2016). Thus, volcanic ash particles detected in infrared satellite measurements after long-distance transportation have a more felsic composition than ash particles sampled near the volcano.

In this work, we use VAC observation data from the Infrared Atmospheric Sounding Interferometer (IASI) and simulate the measured BTSs on the basis of rigorous radiative transfer calculations. In section 2, our numerical method for the radiative

70 transfer calculations is explained. Ash cloud parameters and RI models for the ash particles used in numerical simulations are discussed in section 3, and the selection of IASI pixels, which are used for analysis, is described in section 4. Results of case studies for some VACs are discussed in section 5.

## 2. Infrared spectral simulator Monochromatic-Based Cloud Radiation Model (MBCRM) for volcanic ash cloud
75 **analysis**

To estimate ash cloud parameters and SO₂ gas contents from satellite infrared sounder measurements, a fast and accurate radiative transfer model is needed that can calculate upward channel radiance at the top of the atmosphere (TOA), including multiple light scattering events among ash particles. Furthermore, we examine a number of RI models for volcanic ash materials to simulate the measured BTSs. To meet these requirements, we developed an original radiative transfer code,

80 MBCRM, to simulate infrared sounder measurements. For the basic algorithm of MBCRM, we used the same approach as the

Atmospheric Radiative Transfer Simulator (Buehler et al., 2010). Upward radiance $R_i$ of a sounder channel $i$ at TOA is calculated as the weighted sum of $N$ number of monochromatic radiances $R_{\nu_j}$.

$$R_i = \sum_{j=1}^{N} C_j R_{\nu_j} \tag{1}$$

where $C_j$ is the weighting coefficient $\left(1 = \sum C_j\right)$. Using a diverse atmospheric profile dataset to compare the calculated $R_i$

85   with values derived from exact integration of channel response functions using line-by-line calculations, the monochromatic wavenumber $\nu_j$ and weight $C_j$ were determined, as was the number $N$, using a simulated annealing technique. To simulate the radiance of the 8461 IASI channels, a total of 14,132 monochromatic wavenumber values were determined. The root-mean-square error of $R_i$ for clear-sky conditions was less than the IASI noise equivalent brightness temperature difference, except in the channels of the O$_3$ band at $\nu \approx 1050 \text{ cm}^{-1}$ and the CO$_2$ band at $2200 \leq \nu \leq 2400 \text{ cm}^{-1}$.

90   A plane-parallel single homogeneous layer VAC was assumed for calculations of multiple scattering by cloud particles. The values of $\nu_j$ and $C_j$ in Eq. (1) determined under clear-sky conditions can be applied to calculations in a cloudy atmosphere with high accuracy (Holl et al., 2012), and we used the same formulation of Eq. (1) for radiance calculations in cloudy conditions caused by volcanic ash. For monochromatic radiative transfer calculations at infrared wavelengths, we originally formulated an analytical expression of TOA radiance in which the terms for cloud multiple scattering were described by coefficients

95   depending only on cloud geometry and cloud optical properties. A look-up-table (LUT) of coefficients for various ash cloud conditions was prepared for calculation of monochromatic radiance in advance using the discrete ordinate method with 64 streams. In our benchmark test, the CPU time for TOA radiance calculation using MBCRM over 100 layers of atmosphere and 8461 IASI channels was 0.73 (0.34) sec under cloudy (clear) conditions.

100   **3. Ash cloud parameters for radiative transfer calculations and RI models**

Using LUTs for ash optical properties, numerical simulations of IASI measurements of VACs were conducted using MBCRM. A prolate spheroid shape with a 1:2 axis ratio and a log-normal size distribution (Hansen and Travis, 1974) with a geometric standard deviation of 0.74 (Pavolonis et al., 2013) were assumed for ash particles. The optical properties of the particles were calculated using the T-Matrix method (Mishchenko et al., 2002) for particle effective radii $r_{eff}$ from 0.1 to 20 μm (particle

105   size is defined as the radius of a sphere with equivalent volume). In satellite infrared sounder measurements, volcanic ash mainly affects TOA brightness temperature in the wavenumber range of $\nu \leq 1400 \text{cm}^{-1}$, and LUTs of volcanic ash optical properties were prepared for $640 \text{ cm}^{-1} \leq \nu \leq 1400 \text{ cm}^{-1}$ at an interval of $\Delta\nu = 10 \text{ cm}^{-1}$. The optical properties of each IASI channel were estimated through linear interpolation of the LUT. TOA radiance and brightness temperature were calculated under the assumption that the ash clouds are in thermal equilibrium with the ambient air.

110   For RI models of volcanic ash particles, we used the datasets of Reed et al. (2018) and by Prata et al. (2019) (hereinafter RE2018 and PG2019). Additionally, we prepared datasets using the two RI models MP_A and MP_R. These models were originally described as "andesite" and "rhyolite (obsidian)" models by PL1973, and artificial weak absorption features were added to them. The RI models applied in this work are listed in Table 1, and the characteristics of the models are described below.

115

Table 1: Abbreviations of RI datasets and RI models. The RI models of RE2018 (RE010–RE080) are listed in alphabetical order and labelled with the name of the corresponding volcanic ash sample. Numbers used for RI models based on the PG2019 dataset (PG000–PG100) represent the ratio of non-bridging oxygens to tetrahedrally coordinated cations (NBO/T). The values of NBO/T and SiO2

120   (wt. %) for the RI models of RE2018 are from bulk components of the ash samples and were derived by Prata et al. (2019). MP_A and MP_R are the modified andesite and rhyolite RI models, which were originally proposed as "andesite" and "obsidian from Little Glass Mt. California" by PL1973. The wavenumber dependence of each RI model is plotted in Figs. 1–3.

| Dataset | RI model (original sample) | NBO/T | SiO2 |
|---|---|---|---|
| RE2018<br>Reed et al. (2018) | RE010 (Askja) | 0.13 | 72.35 |
| | RE020 (Aso) | 0.43 | 54.96 |
| | RE030 (Eyjafjallajokull-a) | 0.38 | 60.00 |
| | RE040 (Eyjafjallajokull-b) | 0.40 | 58.85 |
| | RE050 (Grimsvötn) | 0.75 | 50.33 |
| | RE060 (Nisyros) | 0.05 | 74.16 |
| | RE070 (Spurr) | 0.36 | 55.99 |
| | RE080 (Tongariro) | 0.17 | 64.13 |
| PG2019<br>Prata et al. (2019) | PG100 | 1.00 | - |
| | PG090 | 0.90 | - |
| | PG080 | 0.80 | - |
| | PG070 | 0.70 | - |
| | PG060 | 0.60 | - |
| | PG050 | 0.50 | - |
| | PG040 | 0.40 | - |
| | PG030 | 0.30 | - |
| | PG020 | 0.20 | - |
| | PG010 | 0.10 | - |
| | PG000 | 0.00 | - |
| Pollack et al. (1973)<br>(modified) | MP_A (andesite) | | 54.15 |
| | MP_R (rhyolite) | | 73.45 |

### 3.1 Refractive index dataset of Reed et al. (2018): RE2018

Using the assumptions of the Rayleigh continuous distribution of ellipsoids (CDE) scattering model for the sampled ash particles and the Lorentz formulation of the RI to ensure consistency with the Kramers–Kronig relationship, Reed et al. (2018) provided a spectral RI dataset of typical volcanic ash samples at wavelengths of 0.33–19 μm (RE 2018). RI data for eight ash samples from seven volcanoes (Askja, Aso, Eyjafjallajökull-(a) and -(b), Grímsvötn, Nisyros, Spurr, and Tongariro) are available from the Aerosol Refractive Index Archive (http://eodg.atm.ox.ac.uk/ARIA/index.html) as well as in the supporting information of PG2019 (https://doi.org/10.1029/2018JD028679). The spectral RIs of RE2018 over the wavenumber range of $650\ \mathrm{cm}^{-1} \leq \nu \leq 1400\ \mathrm{cm}^{-1}$ are plotted in Fig. 1. In the wavenumber range of $700\ \mathrm{cm}^{-1} \leq \nu \leq 800\ \mathrm{cm}^{-1}$, the RI models of RE2018 showed weak absorption features that are not clearly expressed in the andesite and rhyolite models of PL1973. In previous attempts to simulate sounder-observed BTSs, the calculated BTSs tended to have positive bias in this wavenumber range (Gangale et al., 2010; Clarisse et al., 2013; Ishimoto et al., 2016; Clarisse and Prata, 2016). With the RE2018 RI models, improvements of BTS fitting are expected, although the relationships of chemical composition and volcano type (mafic or felsic) with the absorption index (imaginary part of the complex refractive index: $k$) at $700\ \mathrm{cm}^{-1} \leq \nu \leq 800\ \mathrm{cm}^{-1}$ remain unclear. All RI models of the RE2018 dataset have relatively weak absorption peaks ($k \leq 1.0$) and similar wavenumber dependence of $k$ between 1110 and 1250 $\mathrm{cm}^{-1}$. The individual RI models of RE2018, RE020 (Aso) and RE080 (Tongariro), show similar wavenumber dependence of $k$, although their NBO/T and SiO₂ wt. % values differ significantly. In addition, RE050 (Grímsvötn) has a broad feature of $k$ that differs from other RI models of RE2018.

165

170

175
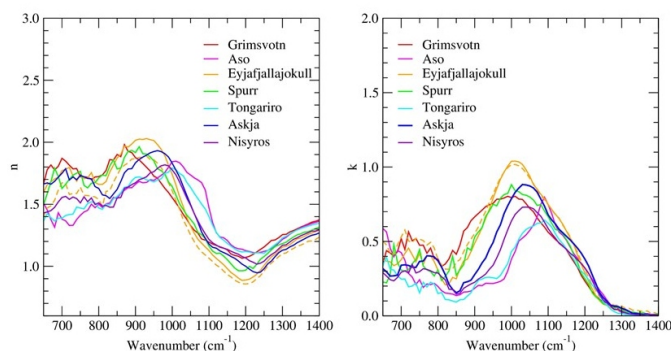
**Figure 1: The real part $n$ (left) and imaginary part $k$ (right) of the RE2018 complex RI models ($RI = n + i \cdot k$). For Eyjafjallajökull**
**ash samples, the yellow solid and dashed lines indicate Eyjafjallajökull-(a) and -(b), respectively. See Table 1 for the abbreviations,**
180   **NBO/T values, and SiO2 wt. % of each RI model.**

### 3.2 RI models parameterised by Prata et al. (2019): PG2019

Using the RE2018 RI dataset and the results of laboratory analysis of the chemical composition of the ash samples, Prata et al.
185   (2019) provided a new parameterisation for the ash RI based on $SiO_2$ content and NBO/T. According to Prata et al. (2019),
NBO/T and $SiO_2$ wt. % in the bulk composition of the ash samples show stronger correlations with the derived RI over a broad
spectral range compared to glass composition. Furthermore, parameterisation using NBO/T provides better results than $SiO_2$
wt. % in both visible and infrared wavelengths. In this study, we used 11 RI models parameterised using NBO/T between 0
and 1 with a step size of 0.1. The $(n, k)$ data for corresponding NBO/T values were calculated using a supporting spreadsheet
190   of Prata et al. (2019), which is available from the publisher's website. Compared to the RE2018 dataset, RI models using
NBO/T parameterisation show simplified wavelength dependences in both the real and imaginary parts of the RI due to the
use of linear regression. However, this simple parameterisation is useful for VAC retrieval based on satellite remote sensing
because an appropriate RI model can be specified in advance based on the assumed chemical composition of the ash material.
In that context, it is essential to verify how well PG2019 RI models reproduce the BTSs of infrared sounder measurements.

195

200

205
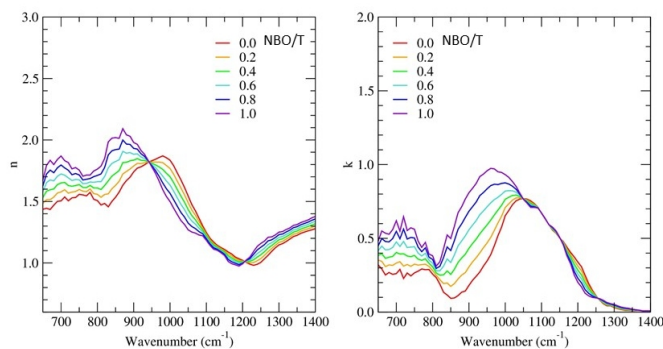
**Figure 2: Same as Fig. 1 but for PG2019 RI models parameterised using NBO/T.**

### 3.3 Modified RI models based on andesite and rhyolite of Pollack et al. (1973): MP_A and MP_R

The two RI models MP_A and MP_R are based on the andesite and rhyolite (obsidian from Little Glass Mt. California) models of PL1973, respectively, and we artificially applied features of weak absorption in the wavenumber range of 700–850 cm$^{-1}$

210 to the absorption index $k$ of each model, referring to the results of BTS analysis reported by (Gangale et al., 2010; Ishimoto et al., 2016). These RI models were used for comparisons to the results of BTS simulations using RI models based on the RE2018/PG2019 datasets.

215

220
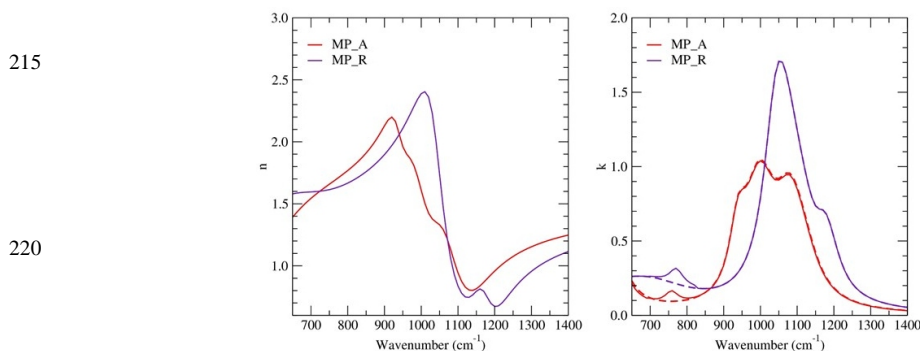
225 **Figure 3: Same as Fig. 1 but for the MP_A (red) and MP_R (blue) models. These RI models are based on the andesite and rhyolite models of PL1973, respectively, with artificial modification of the absorption index $k$ in the wavenumber range of 700–850 cm$^{-1}$ (original $k$ values are indicated with dashed lines).**

230 ### 4. IASI ash cloud data

To identify the optimal RI models by comparing measured and simulated BTSs, continuous data from an infrared sounder that covers the wavenumber range of 650–1400 cm$^{-1}$ is desirable, and VAC data collected by IASI were used in this work. The IASI Level-1C granule data were acquired from the National Oceanic and Atmospheric Administration Comprehensive Large Array-Data Stewardship System (https://www.avl.class.noaa.gov/saa/products/). As a primary condition for BTS analysis, the

235 brightness temperature difference between 10.7 μm (934.5 cm$^{-1}$) and 12.2 μm (819.5 cm$^{-1}$) ($\Delta TB_{split} \equiv TB_{10.7} - TB_{12.2}$) was used, and pixels with $\Delta TB_{split} < -2$ K for VACs over the ocean were selected. For discriminating the results of BTS simulations from different RI models using radiative transfer calculations, VAC pixels with more negative values of $\Delta TB_{split}$ are better, as the BTSs of such pixels shows distinct wavenumber dependence due to absorption in the infrared window region. The value $-2$ K was chosen as the minimum requirement for discriminating the difference in BTSs between the results of

240 different RI models. We excluded VAC data over land due to large uncertainties in spectral surface emissivity and surface temperature.

Our radiative transfer model MBCRM conducts forward calculations for a single layer of VAC with no contamination from meteorological clouds (MCs) consisting of water or ice particles. Because MC contamination in VAC pixels can cause large estimation errors for ash cloud parameters and RI models (Kylling et al., 2015), contaminated pixels must be excluded to

245 ensure the validity of the estimated RI model based on the results of our BTS analysis. In the case of VAC covered with dense MC layers, most measured pixels are rejected due to the condition $\Delta TB_{split} < -2$ K. On the other hand, if a portion of the pixel area is covered by MC or if the VAC is located above the MC layers, the MC can cause a negative bias in the measured

BTS and still meet $\Delta TB_{split} < -2$ K. As a result, large errors may occur for the estimation of ash cloud parameters under the assumption of a single VAC layer. Furthermore, the detailed wavelength dependence of the BTS for such contaminated pixels may differ from that of the pure VAC. For these reasons, we used VAC data from daytime IASI measurements, and pixels that were presumed to be affected by MC were excluded through reference to visible true-colour imagery for the same area from the Moderate Resolution Imaging Spectroradiometer (MODIS) onboard the Terra and Aqua satellites. MODIS images were provided by the Level-1 and Atmosphere Archive & Distribution System Distributed Active Archive Center, and are available online (https://atmosphere-imager.gsfc.nasa.gov/images/l1b-granules). The visible true-colour image product of the Japanese geostationary meteorological satellite Himawari-8 Advanced Himawari Imager (AHI) (Bessho et al., 2016) was also used for volcanic eruptions since 2015 in the coverage area of Himawari-8 (images were downloaded from the Japan Aerospace Exploration Agency Himawari Monitor homepage: https://www.eorc.jaxa.jp/ptree/index.html). Because we used daytime IASI measurements that could be referenced to MODIS images, the number of VAC pixels available for our analysis was significantly reduced. Furthermore, the evaluation of IASI pixels using MODIS visible images does not always exclude MC contamination due to the time difference between IASI and MODIS measurements as well as the difference in sensor spatial resolution. Therefore, we added another condition for IASI pixels in our analysis. As the temperature of the MC layer is generally lower than that of the sea surface at the same geographic location, a VAC above an MC layer tends to have a lower infrared brightness temperature than a VAC with no MC if the cloud parameters of the VAC are the same. Using brightness temperature at wavenumber $\nu_a$, where the measured brightness temperature is maximised in the region of $750 \text{ cm}^{-1} \leq \nu \leq 900 \text{ cm}^{-1}$ due to a local minimum of the absorption index $k$, the difference $\Delta TB_{clr}$ between the brightness temperatures of clear sky $TB_{clr}(\nu_a)$ and ash clouds $TB_{obs}(\nu_a)$ was defined as $[\Delta TB_{clr} \equiv TB_{clr}(\nu_a) - TB_{obs}(\nu_a)]$. The value of $\nu_a$ was derived from VAC measurements and $TB_{clr}(\nu_a)$ was calculated using our forward model. Then, a threshold of $\Delta TB_{clr}$ was set according to the value of $\Delta TB_{split}$. Figure 4 shows a plot of $TB_{clr}(\nu_a)$ with respect to $\Delta TB_{split}$ in 1171 IASI pixels of VAC measurements for the volcanic eruptions listed in Table 2. The pixels are selected based on the primary condition $\Delta TB_{split} < -2$K over ocean areas, including night-time data. The clear-sky brightness temperature $TB_{clr}(\nu_a)$ was calculated using atmospheric profiles, sea surface temperature, and atmospheric pressure at the surface from the results of global analysis (GANAL) via numerical modelling by the Japan Meteorological Agency. In Fig. 4, pixels are discriminated between Eyjafjallajökull (blue) and other volcanic eruptions (red), and the two datasets in the plot show similar distribution patterns. If a pixel of pure VAC observation is contaminated with MC, the negative value of $\Delta TB_{split}$ is likely to become smaller, while the value of $\Delta TB_{clr}$ is likely to increase. Therefore, the upper right data in Fig. 4 may have higher probabilities of MC contamination than the lower left data on the plot. In our retrieval analysis, a threshold value of $\Delta TB_{clr}$ (K) was defined to reduce the fraction of MC-contaminated pixels:

$$\Delta TB_{clr.th} \equiv -2 \cdot \Delta TB_{split} + 6 \qquad (2)$$

and $\Delta TB_{clr} < \Delta TB_{clr.th}$ was applied as an additional retrieval condition. The coefficients of Eq. (2) were artificially determined, and approximately 35% of all pixels with $\Delta TB_{split} < -2$K were rejected due to this condition for the Eyjafjallajökull VAC shown in Fig. 4. The aim of this condition is to reduce the fraction of MC-contaminated pixels in our analysis; this threshold cannot be used to determine whether an individual pixel is contaminated with MC. Even for a pure VAC of a single homogeneous layer, $\Delta TB_{clr}$ may be greater than $\Delta TB_{clr.th}$ depending on the cloud parameters of the VAC. In addition to MC contamination, the negative value of $\Delta TB_{split}$ decreases and $\Delta TB_{clr}$ increases for VACs with larger particle sizes and optical depths, as shown in the scatter plot of Fig. 4, which is essentially the same as the split-window plotting method (Prata, 1989; Wen and Rose, 1994; Prata and Grant, 2001) with the vertical and horizontal axes switched. Thus, the retrieval condition of Eq. (2) aims to select pixels showing sparse VACs comprised of small particles.

290

295

300
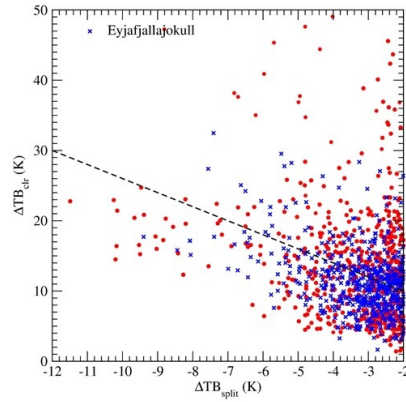
**Figure 4: Estimated brightness temperature difference $\Delta TB_{clr}$ for VAC pixels of $\Delta TB_{split}$ measured with IASI. In total, 1171 pixels**
305 **of $\Delta TB_{split} < -2K$ from the volcanic eruptions listed in Table 2 were used. Data for Eyjafjallajökull eruptions (6–16 May 2010) are**
**coloured blue. The dashed line indicates the threshold of $\Delta TB_{clr}$ from Eq. (2) used for retrieval analysis in this work.**

For retrieval analysis, we selected up to 10 VAC pixels with large negative values of $\Delta TB_{split}$ from a granular dataset of IASI
310 measurements. Radiative transfer calculations and BTS simulations for the selected VAC pixels were conducted using
assumptions for three VAC parameters, pressure height of cloud top $P_{top}$, optical depth at wavelength 11 μm ($\nu =$
907.488 $cm^{-1}$), and effective radius of ash particles $r_{eff}$, which were retrieval variables, and using the temperature/water
vapour profiles and sea surface temperature/pressure from GANAL as fixed values. We set the pressure height of the cloud
base $P_{base}$ to $P_{base} = P_{top} + 100$ hP$_a$ for simplicity. For the ozone profile, the total column of ozone was treated as a retrieval
315 variable, and the relative values for the initial ozone profile from GANAL were fixed. A homogeneous volcanic SO$_2$ gas layer
with a pressure difference of 100 hP$_a$ between the top and base was assumed, with the pressure height of the layer top and
total column used as variables. The estimated values of the retrieval variables were those for which the root mean square
(RMS) between measured and calculated brightness temperatures ($TB^{obs}$ and $TB^{cal}$) in the assumed channels of number N is
minimised. The optimal RI models were generally identified by comparing the RMS values of various RI models.

320 $$RMS = \sqrt{\frac{1}{N}\sum_{i=1}^{N}(TB_i^{obs} - TB_i^{cal})^2} \qquad (3)$$

Retrieval calculations were conducted using the scattering properties for ash particles derived from the selected RI model and
data for IASI channels of 650 $cm^{-1} \le \nu \le 1400$ $cm^{-1}$ with the following procedure:

a) VAC parameters $(P_{top}, r_{eff}, \tau_c)$ are estimated using $TB^{obs}$ and $TB^{cal}$ for channels excluding the ozone band of
980 $cm^{-1} \le \nu \le 1080$ $cm^{-1}$ and SO$_2$ bands of 1100 $cm^{-1} \le \nu \le 1210$ $cm^{-1}$ and 1320 $cm^{-1} \le \nu \le 1395$ $cm^{-1}$.

325 b) The total columns of ozone and SO$_2$ are estimated using the channels 980 $cm^{-1} \le \nu \le 1080$ $cm^{-1}$ for ozone and
1320 $cm^{-1} \le \nu \le 1395$ $cm^{-1}$ for SO$_2$, assuming the VAC parameters $(P_{top}, r_{eff}, \tau_c)$ as fixed values. The wavenumbers
1100 $cm^{-1} \le \nu \le 1210$ $cm^{-1}$ are excluded from estimation of the SO$_2$ column because the brightness temperature of these
channels is strongly influenced by the applied ash RI model.

c) The RMS for the channels 750 $cm^{-1} \le \nu \le 1400$ $cm^{-1}$ is then calculated, considering the estimated VAC, ozone, and SO$_2$
330 parameters as fixed. We excluded the range of 650 $cm^{-1} \le \nu < 750$ $cm^{-1}$ to avoid RMS values related to error in the
GANAL atmospheric profiles.

d) Processes a–c are conducted for all RI models.

The date and number of pixels in the selected IASI data for eruptions from 11 volcanoes are listed in Table 2. The average value of the wavenumber $\bar{\nu}_a$ at the local maximum of brightness temperature and $SiO_2$ wt. % of tephra samples from the literature are included for reference. In particular, $\nu_a$ is related to the minimum of the absorption index $k$, and has been reported as an important parameter for identifying ash material from infrared sounder measurements (Gangale et al., 2010; Clarisse et al., 2013; Clarisse and Prata, 2016). Using a total of 21 RI models, which are listed in Table 1, the minimum RMS of brightness temperature in the wavenumber range $750 \text{ cm}^{-1} \leq \nu \leq 1400 \text{ cm}^{-1}$ was determined for each RI model. In the following sections, we discuss the results for the best fitting (optimal) RI models determined from RMS values for the volcanic events in Table 2. The detailed results for minimal RMS and VAC parameters $\left(P_{top}, r_{eff}, \tau_c\right)$, ash top height $h_{top}$ estimated from $P_{top}$ and the GANAL profile, and total column $SO_2$ for each IASI pixel are provided in the Supplemental Material. In this study, we assume that the ash material ejected from a given volcano remains the same throughout the period of each eruption event in Table 2, and also assume that the optimal RI model is the one for which the sum of the RMS for all pixels of a given volcano is smallest. Even if the total RMS was the smallest, we rejected an RI model as unrealistic if the converged values of $r_{eff}$ were the smaller than 0.2 μm for many pixels in the retrieval analyses. In addition to the differences among RI models, the size of ash particles effectively changes the wavelength dependence of the simulated BTS (Clarisse and Prata, 2016; Ishimoto et al., 2016), and small values of $r_{eff}$ tend to be estimated when a relatively mafic RI model is used with low $SiO_2$ wt. % or large NBO/T values. The relationship between the estimated $r_{eff}$ value and the RI model in the retrieval analysis is discussed in section 5.1.

**Table 2: Volcanic eruption events used for BTS analysis of IASI measurements and the results of the optimal RI models. The optimal RI models are identified through comparison between measured and simulated BTSs for IASI pixels on the date "Date." Two RI models in the column "Optimal RI model" indicate that the results of BTS fitting were almost the same. The average wavenumber $\bar{\nu}_a$ at which the measured brightness temperature is maximised in the range of $750 \text{ cm}^{-1} \leq \nu \leq 900 \text{ cm}^{-1}$ and SiO2 wt. % values of ash and pumice samples from the literature are added. [1] Turner et al. (2013), [2] Romero et al. (2016), [3] Deguine et al. (2020), [4] Reed et al. (2018), [5] Prata et al. (2019), [6] Maeno et al. (2019), [7] http://www.eri.u-tokyo.ac.jp/PREV_HP/outreach/eqvolc/201101_shinmoe/eng/ , [8] Sano et al. (2016), [9] Castro et al. (2013), [10] Prata and Lynch (2019), [11] Rybin et al. (2011), [12] Plechova et al. (2011)**

| Name of volcano | Location of Volcano (Lat., Lon.) | | Country | Date (yyyymmdd) | IASI pixels | Optimal RI model | $\bar{\nu}_a(\text{cm}^{-1})$ | SiO2 |
|---|---|---|---|---|---|---|---|---|
| Bezymianny | 55.972 | 160.595 | Russia | 20190315-16 | 2 | PG020 | 826.8 | 56.8[1] |
| Calbuco | -41.33 | 287.382 | Chile | 20150424 | 25 | PG020, (PG050) | 829.2 | 55[2],56.3[3] |
| Eyjafjallajökull | 63.633 | 340.367 | Iceland | 20100506-12 | 50 | PG040, RE030 | 819.3 | 58-60[4,5] |
| Grimsvötn | 64.416 | 342.684 | Iceland | 20110522-23 | 11 | PG070, RE050 | 817.2 | 50.6[5] |
| Kelut | -7.93 | 112.308 | Indonesia | 20140214 | 4 | PG010, PG000 | 860.4 | 55-56[6] |
| Kirishimayama | 31.934 | 130.862 | Japan | 20110127 | 9 | RE080, RE020 | 830.4 | 57, 62[7] |
| Nishinoshima | 27.247 | 140.874 | Japan | 20200731 | 18 | PG070, RE070 | 827.3 | 58-62[8] |
| Puyehue-Cordon | -40.59 | 287.883 | Chile | 20110606 | 39 | PG000 | 859.9 | 69.6[9] |
| Rinjani | -8.42 | 116.47 | Indonesia | 20151106 | 1 | PG030 | 819.5 | 64.3[10] |
| Sarychev_peak | 48.092 | 153.2 | Russia | 20090616 | 1 | PG100, RE050 | 788.7 | 54[11] |
| Zhupanovsky | 53.589 | 159.15 | Russia | 20160212-13 | 4 | PG020 | 830.3 | 46-54[12] |

## 5. Refractive index models estimated through IASI measurement simulation

375  Selected IASI measurements for the eruption events of 11 volcanoes and the results of the optimal RI models are listed in Table 2. Ranking plots for the results of RMS analysis for each measurement pixel are shown in Fig. 5. Ranking based on the smallest RMS was conducted for the 21 RI models. Detailed results for each RI model in each pixel, including the minimum RMS, estimated ash cloud parameters $(P_{top}, h_{top}, r_{eff}, \tau_c)$, and $SO_2$ column, are provided in the Supplemental Material. The RI models from the PG2019 dataset were selected as optimal for 10 volcanic events. Furthermore, high-ranking RI models

380  tended to converge at a specific value of NBO/T in the PG2019 dataset. This result suggests that NBO/T, which can be determined from the chemical composition of the ash, is an effective indicator of the appropriate RI model for satellite VAC analysis. On the other hand, the andesite model of PL1973 (MP_A) was not selected as the best RI model despite having a better RMS than the original andesite model of PL1973. This finding clearly shows that high-accuracy BTS simulations can be achieved using the novel RI models of RE2018 and PG2019. The results of VAC analysis for individual volcanoes are

385  discussed in the following subsections. Typical results of the BTS simulations are shown in the figures, and the estimated VAC parameters, $SO_2$ column, and RI model used for each simulation are summarised in Table 3.
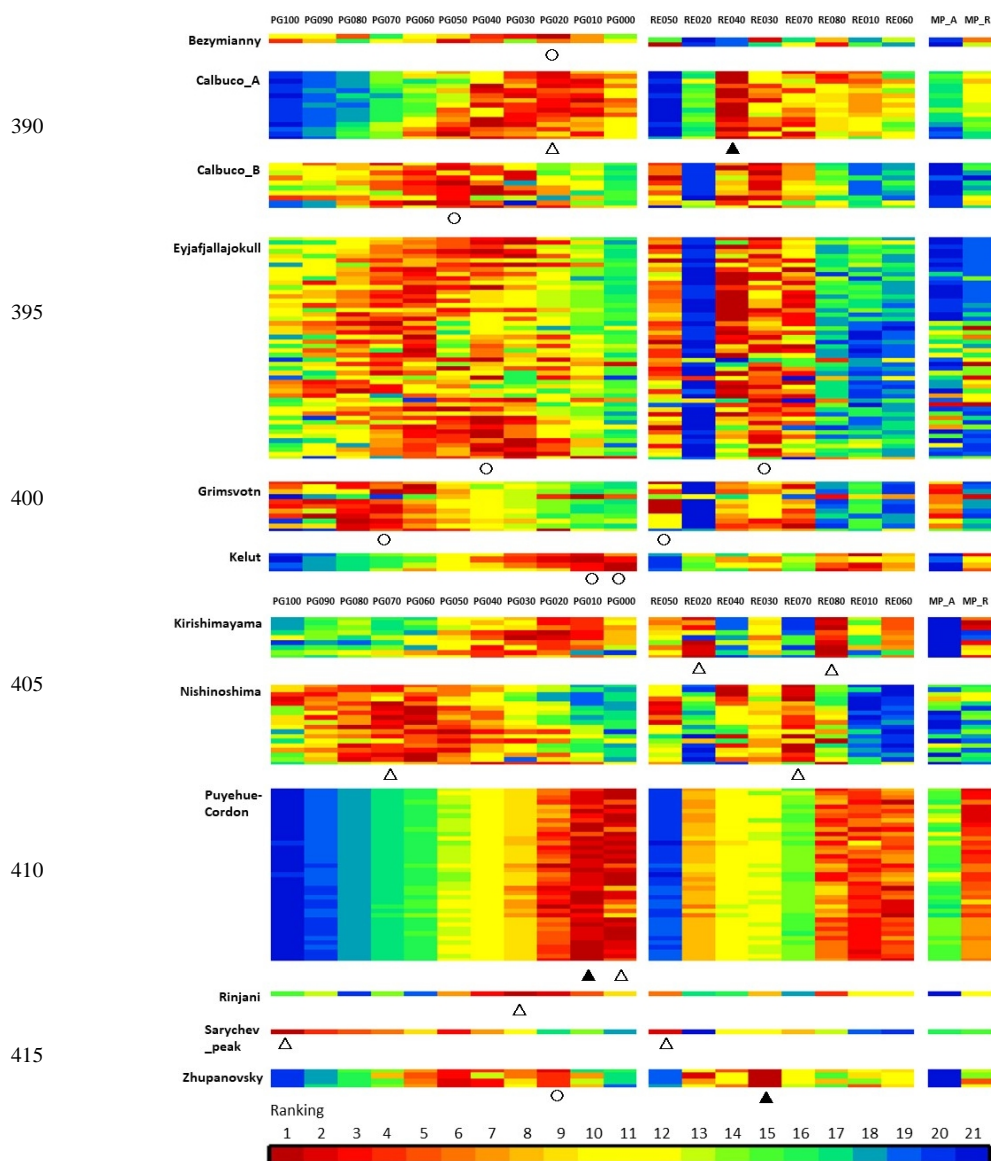
**Figure 5: Ranking plots showing the results of BTS simulations for the pixels used for the IASI ash cloud measurements in Table 2.**
420 **The ranking of the 21 RI models is in ascending order of the RMS values between the measured and simulated BTSs. Results for different pixels are shown on different lines, which are ordered by the date and time of IASI granule measurements from top to bottom. The 11 RI models using the PG2019 dataset are arranged based on NBO/T values (0.0 to 1.0 in steps of 0.1 from right to left), while the eight RI models using the RE2018 dataset and two RI models from PL1973 (MP-A/-R) are arranged based on SiO2 wt. % (Table 1). The optimal RI model for the volcano was determined from sum of RMS values for the corresponding measurement pixels. An open circle (◯) indicates that the BTS simulated using the optimal RI model provides a good fit to the measured BTS,**
425 **and other optimal RI models are indicated by open triangles (△). The RI model with a solid triangle (▲) resulted in the smallest sum of RMS values, but was rejected as an optimal RI model because many estimated $r_{eff}$ values were less than 0.2 μm.**

**Table 3: Locations of IASI pixels, applied RI models, retrieved VAC parameters ($h_{top}, r_{eff}, \tau_c$), and SO₂ columns (in Dobson units)**
430 **for BTS simulations of typical VAC measurements ("Figure No.").**

| Figure No. | Volcano | Pixel location (lat., lon.) in deg. | RI model | Top height (km) | Effective radius (μm) | Optical thickness @11 μm | SO2 column (DU) |
|---|---|---|---|---|---|---|---|
| 6c | Eyjafjallajökull | (63.146N, 15.261W) | RE030 | 5.97 | 0.84 | 2.24 | 34.4 |
|  |  |  | PG040 | 6.23 | 1.18 | 2.08 | 54.4 |
| 6f | Eyjafjallajökull | (52.549N, 24.075W) | RE030 | 3.67 | 0.84 | 1.34 | 0.0 |
|  |  |  | PG040 | 4.30 | 1.30 | 0.96 | 0.0 |
| 8c | Grimsvötn | (61.390N, 21.484W) | RE050 | 1.82 | 0.84 | 1.07 | 0.0 |
|  |  |  | PG070 | 1.74 | 1.50 | 1.15 | 0.0 |
| 9c | Calbuco (A) | (35.336S, 55.051W) | PG020 | 12.98 | 0.37 | 0.14 | 49.0 |
| 9f | Calbuco (B) | (32.592S, 75.050W) | PG050 | 4.47 | 0.57 | 0.80 | 1.3 |
|  |  |  | PG020 | 4.70 | 1.36 | 0.68 | 0.0 |
| 10c | Kirishimayama | (31.079N, 136.500E) | RE020 | 4.00 | 2.80 | 1.11 | 0.0 |
|  |  |  | RE080 | 3.02 | 2.20 | 1.38 | 0.0 |
| 10f | Nishinoshima | (26.719N, 141.167E) | RE070 | 3.78 | 0.39 | 0.88 | 0.0 |
|  |  |  | PG070 | 3.68 | 0.29 | 0.99 | 0.0 |
| 11d | Kelut | (9.101S, 110.513E) | PG000 | 11.02 | 1.18 | 0.61 | 44.0 |
| 12d | Puyehue-Cordon | (27.136S, 25.178W) | PG000 | 7.29 | 0.24 | 0.33 | 4.4 |
| 12g |  | (41.238S, 62.692W) | PG000 | 10.23 | 0.16 | 0.33 | 8.7 |
| 13c | Bezymianny | (55.488N, 164.850E) | PG020 | 1.58 | 1.30 | 0.92 | 31.4 |
| 13f | Zhupanovsky | (52.949N, 161.367E) | PG030 | 1.66 | 0.24 | 0.76 | 34.9 |
| 13i | Rinjani | (8.935S, 116.035E) | PG030 | 3.62 | 3.09 | 1.23 | 0.0 |
| 13l | Sarichev_peak | (49.033N, 152.698E) | RE050 | 4.08 | 0.69 | 3.60 | 28.2 |
|  |  |  | PG100 | 3.98 | 0.57 | 4.65 | 28.3 |

### 5.1 Eyjafjallajökull

In the case of the Eyjafjallajökull eruptions in 2010, RI models developed from the results of laboratory analysis of ash samples were provided by RE2018 and data of IASI measurements were obtained. Simulations of the measured BTS were conducted using 50 BTS datasets for IASI pixels that satisfied our retrieval conditions over the period of 6–12 May 2010. Overall, the RI
455 models of NBO/T = 0.2–0.5 (PG020–PG050) for the PG2019 dataset and the RI model Eyjafjallajökull-(a) (RE030) using the RE2018 dataset showed good BTS fitting results. Specifically, RE030 and PG040 gave similar values for the smallest sum of RMS values over the 50 total pixels. This result is reasonable if the ash particles measured by IASI were composed of the same material as the ash particles sampled for laboratory analysis in RE2018, and the results also suggest that parameterisation using NBO/T works well for the PG2019 RI model. Furthermore, this result supports the feasibility of estimating ash RI from satellite

460   infrared sounder measurements. Typical results of BTS analysis for the Eyjafjallajökull VAC are shown in Fig. 6. For these
IASI measurements, true-colour images from the MODIS product (Fig. 6a and d) near the IASI measurement time were
obtained. Through comparison with the colour image shown in Fig. 6a, the influence of MCs appears small in the vicinity of
IASI pixels with highly negative $\Delta TB_{split}$ values in Fig. 6b. The results of BTS simulation with RE030 and PG040 were very
similar and agreed well with the measured BTS, although some differences occurred for the estimated VAC parameters

465   $(h_{top}, r_{eff}, \tau_c)$ (Table 3). Because PG040 is parameterised by NBO/T = 0.4 and this NBO/T value is close to that of the
Eyjafjallajökull-(a) ash sample at 0.38, the wavenumbers of the local minimum and local maximum of the absorption index $k$
obtained using PG040 are similar to those of RE030 (Figs. 1 and 2). Thus, the results of BTS simulations shown in Fig. 6c
arise from the similarity of the spectral pattern of $k$ between PG040 and RE030. Another Eyjafjallajökull VAC was located
more than 1000 km from the volcano on 9 May 2010 (Fig. 6d–f). In IASI measurements, pixels with highly negative values

470   of $\Delta TB_{split}$ are present in the area of $51°\,N \le lat \le 54°\,N, 20°\,W \le lon \le 28°\,W$ (circle in Fig. 6e); a faint VAC with
sparse broken clouds was inferred in this area from the MODIS colour image, and an ash optical thickness of 0.15–0.20 at
visible wavelengths was estimated by Ventress et al. (2016)). Figure 6f shows the results of BTS simulation for one of the nine
selected pixels in this area. As shown in Fig. 6c, the BTSs simulated using PG040 and RE030 agree well with the measured
values, and the effect of MC contamination on the measured BTS appears minor. The average VAC parameter values over the

475   nine pixels were $(\bar{h}_{top}, \bar{r}_{eff}, \bar{\tau}_c) = (3.45\ km, 0.83\ \mu m, 1.42)$ for PG040 and $(\bar{h}_{top}, \bar{r}_{eff}, \bar{\tau}_c) = (3.29\ km, 0.70\ \mu m, 1.60)$ for
RE030. Although the values of $h_{top}$ and $r_{eff}$ are smaller than those obtained by Ventress et al. (2016) , which were optimally
estimated using IASI data in the same area and an Eyjafjallajökull RI model ($h_{top} \ge \sim 4\ km$ and $r_{eff} \ge \sim 2\ \mu m$; from Fig. 5
in Ventress et al., 2016), they are consistent with the mode values of the estimated $h_{top}$ and $r_{eff}$ histograms based on IASI
data from the same day (Ventress et al., 2016). In our analysis of 50 total pixels showing the Eyjafjallajökull VAC from 6–12

480   May, the average value of the effective radius $\bar{r}_{eff}$ was 1.08 μm (0.96 μm) with the PG040 (RE030) RI model, which agrees
with the results from aircraft observations that $r_{eff}$ is in the range of 0.87–1.19 μm (Turnbull et al., 2012; Ventress et al.,
2016).
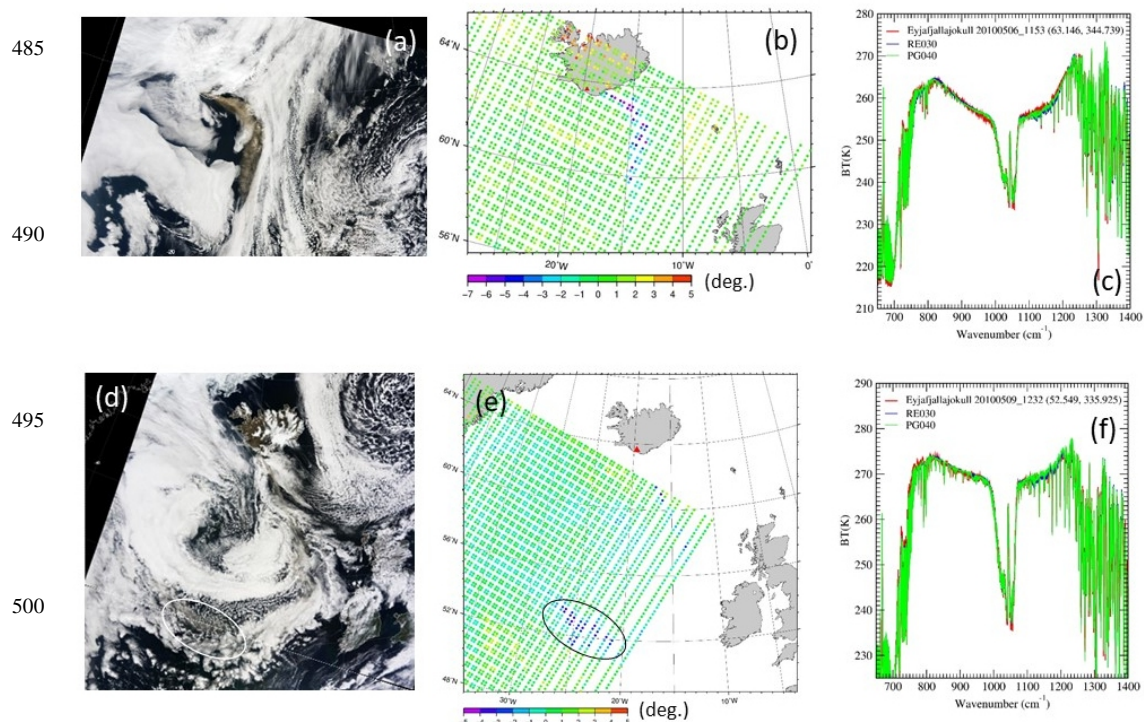
**Figure 6: Examples of BTS analyses of the Eyjafjallajökull VAC on 6 May 2010 (a–c). (a) MODIS true-colour image at 11:55 UTC**
**and (b) brightness temperature difference $\Delta TB_{split}$ measured with IASI at 11:53 UTC. (c) BTS of IASI measurement at $(lat, lon) =$**
505 **$(63.146° \, N, 15.261° \, W)$ (red), and results of BTS simulations using the RI models RE030 (blue) and PG040 (green). (d–f) Same as**
**(a–c), but for the VAC on 9 May 2010. The MODIS colour image is a composite from 12:25–12:30 UTC (d) and IASI $\Delta TB_{split}$ is**
**calculated at 12:32 UTC (e). The area of highly negative $\Delta TB_{split}$ is indicated with circles in (d and e). (f) Measured and simulated**
**BTSs for the IASI pixel at $(lat, lon) = (52.549° \, N, 24.075° \, W)$. The retrieved VAC parameters and SO2 column for each BTS**
**simulation are listed in Table 3.**

510

Using the retrieval results for 50 pixels of Eyjafjallajökull VAC measurements under various RI models (PG070, PG040, and

PG010), the dependence of the RI model on the estimated VAC parameters $\left(h_{top}, r_{eff}, \tau_c\right)$ was investigated (Fig. 7a–c).

Although the estimated VAC parameters differed among the RI models tested, no systematic bias was apparent for $h_{top}$ or $\tau_c$.

515 On the other hand, the results for $r_{eff}$ show a strong dependence on RI model selection (Fig. 7b). Within the PG2019 dataset,

small values of $r_{eff}$ tend to be estimated for mafic RI models with large NBO/T. By contrast, relatively large $r_{eff}$ values were

derived for felsic RI models. Similar dependence of RI models on estimated $r_{eff}$ was also confirmed for our VAC retrievals

related to other volcanic events listed in Table 2. Using a pixel with small differences in retrieved $h_{top}$ and $\tau_c$ among the three

RI models (pixel no. 30), the results of BTS simulations with different $r_{eff}$ values using PG070 and PG010 are plotted in Fig.

520 7d and 7e, respectively. If we assume that the RI model of PG040 is adequate for Eyjafjallajökull ash material and that the

retrieval result $r_{eff} = 1.07$ μm using PG040 is close to the true value, a positive bias of the simulated BTS in the region of

$900 \, \text{cm}^{-1} \leq \nu \leq 1230 \, \text{cm}^{-1}$ occurs, except within the ozone band, when we use a more mafic RI model (PG070) than PG040

with the same $r_{eff}$ value (blue line of Fig. 7d). The positive bias of the BTS is mitigated by applying a smaller value of $r_{eff}$

in the BTS simulation (green line). By contrast, a negative bias of the BTS occurs in the same wavenumber range (blue line of

525 Fig. 7e) when we use a more felsic RI model (PG010), and fitting of the calculated BTS improves when a larger $r_{eff}$ value is

used for the ash particles (green line of Fig. 7e). Thus, the retrieval results of $r_{eff}$ are sensitive to the wavenumber dependence

of the particle absorption property around $900 \, \text{cm}^{-1} \leq \nu \leq 1230 \, \text{cm}^{-1}$. Therefore, selection of the proper RI model is

essential, especially for the estimation of $r_{eff}$. This result also suggests that RI model selection may have a strong influence

on the estimation of ash column density, as it is directly related to the retrieved $r_{eff}$ (Pavolonis et al., 2013). In our BTS analysis

530 of the Eyjafjallajökull VAC, PG040 and RE030 were selected as the optimal RI models as their fitting results were better than

those of other RI models in wavenumber regions other than $900 \, \text{cm}^{-1} \leq \nu \leq 1230 \, \text{cm}^{-1}$ (in particular, $750 \, \text{cm}^{-1} \leq \nu \leq$

$900 \, \text{cm}^{-1}$).

535

540

545
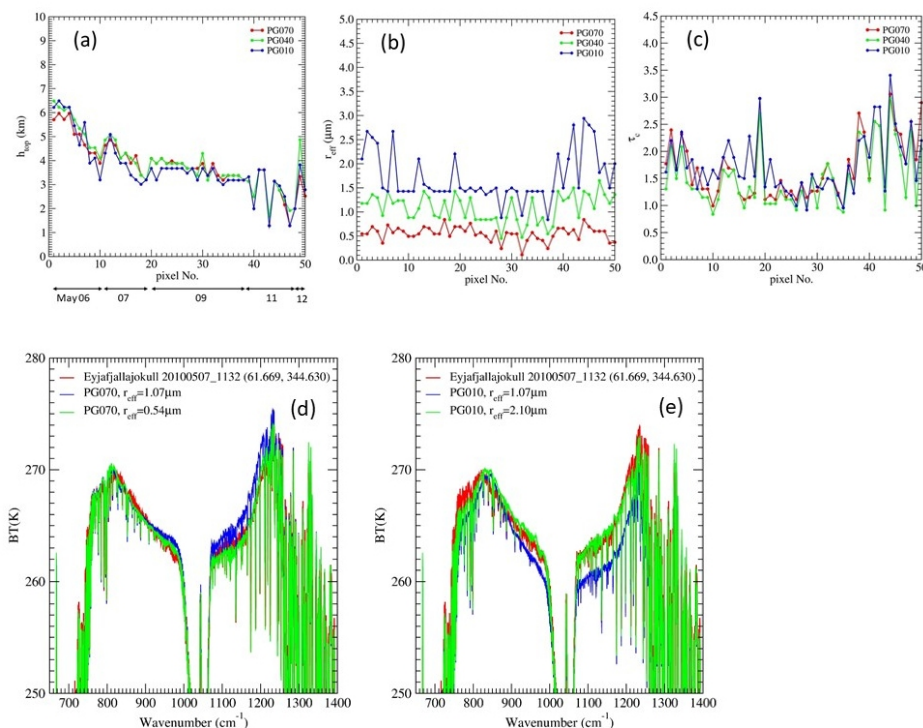
**Figure 7: The ash cloud parameters cloud top height $h_{top}$ (a), particle effective radius $r_{eff}$ (b), and optical thickness $\tau_c$ (c) estimated from our BTS analysis of 50 IASI pixels for Eyjafjallajökull VAC measurement. Observation dates corresponding to the serial**

570 **number of the pixel are shown in the lower part of (a). (d, e) BTS results for three RI models: PG070 (red), PG040 (green), and PG010 (blue). (d) and (e) show examples of measured and calculated BTSs using IASI data for pixel no. 30 [7 May 11:32 UTC, $(lat, lon) = (61.669° N, 15.370° W)$]. The blue line in (d) indicates the BTS calculated using the PG070 RI model and the same VAC parameters as the PG040 RI model $(h_{top}, r_{eff}, \tau_c) = (4.86 \text{ km}, 1.07 \text{ μm}, 1.89)$, while the green line shows the BTS calculated after changing the $r_{eff}$ value from $1.07$ μm to $0.54$ μm. (e) is the same as (d) but using the PG010 RI model and VAC parameters**

575 $(h_{top}, r_{eff}, \tau_c) = (4.86 \text{ km}, 1.07 \text{ μm}, 1.89)$ **(blue line) and $(4.86 \text{ km}, 2.10 \text{ μm}, 1.89)$ (green line).**

### 5.2 Grímsvötn

In addition to Eyjafjallajökull, an RI model from the laboratory experiments of RE2018 and IASI measurements of ash clouds

580 were obtained for the Grímsvötn eruptions in May 2011. From IASI data for the Grímsvötn VAC, one pixel at 12:08 UTC on 22 May and 10 pixels at 11:47 UTC on 23 May were selected for our BTS analysis. The measured IASI pixels of $\Delta TB_{split} < -2\text{K}$ on 23 May (Fig. 8b) were estimated to have low MC contamination based on the MODIS colour image taken at 12:05 UTC (Fig. 8a). Moreover, from this MODIS colour image, MCs in the area of the VAC were determined to be located at higher altitudes than the VAC (Prata et al., 2017b), suggesting that the MC-contaminated pixels were effectively excluded from the

585 target pixels in our BTS analysis.

For the VAC of Grímsvötn eruptions, the BTS based on IASI measurements was reported to produce good simulation results using the basalt RI model of PL1973 (Newman et al., 2012). The results of our BTS simulations showed that a small RMS was obtained for the PG070 RI model using the PG2019 dataset, and RI models derived from Grímsvötn (RE050) and Spurr (RE070) ash samples within RE2018 dataset returned relatively small RMS values. Absorption features related to $SO_2$ gas

590 were not present in the BTSs of the 11 analysed pixels, in accordance with the report of $SO_2$ gas separation from the ash clouds (Prata et al., 2017b), and thus PG070 and RE050 were selected as the optimal RI models based on their total RMS scores. The estimate of NBO/T for the Grímsvötn ash sample is 0.74–0.75, which is the highest value within the RE2018 dataset (Prata et al., 2019). Because the PG2019 dataset is derived from NBO/T parameterisation using the RE2018 dataset, the wavelength dependence of PG070 is similar to that of RE050. As a result, similar VAC parameters were estimated for PG070 and RE050,

595 and the average values over 11 pixels $\left(\bar{h}_{top}, \bar{r}_{eff}, \bar{\tau}_c\right) = (1.58\,\text{km}, 0.93\,\mu\text{m}, 2.06)$ were almost identical for these two RI models. This result for $r_{eff}$ generally agrees with published results for a Grímsvötn ash sample (1.1 μm) (Reed et al., 2018). For cloud top height, Moxnes et al. (2014) estimated $h_{top} \le 4$ km through analysis of IASI data, and similar results for cloud height were obtained using the Inversion Technique for Emission Modelling (Harvey et al., 2020). Although our results for $h_{top}$ are smaller, they are generally consistent with previous research. An example of the results from BTS simulations is

600 shown in Fig. 8c. Due to the small $SO_2$ contribution, the BTS in the range of $1100\,\text{cm}^{-1} \le \nu \le 1210\,\text{cm}^{-1}$ is mainly driven by the optical properties of ash particles, and the difference in the BTSs of PG070 and RE050 was small in this wavenumber range.

605

610
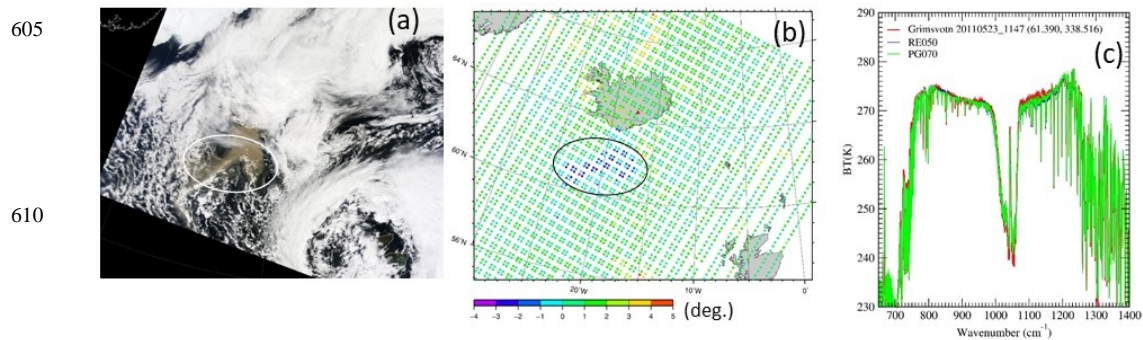
**Figure 8: A Grímsvötn VAC on 23 May 2011, shown in a MODIS true-colour image taken at 12:05 UTC (a), $\Delta TB_{split}$ from IASI measurements at 11:47 UTC (b), and the BTS of the IASI pixel at $(lat, lon) = (61.390°\,\text{N}, 21.484°\,\text{W})$ (red) (c). The results of BTS simulations using RE050 (blue) and PG070 (green) are also shown in (c).**

620 The best RI models for simulating the observed BTSs of the Eyjafjallajökull and Grímsvötn VACs had similar NBO/T values to ash samples from the same volcanic eruptions. This result provides evidence that the BTS of volcanic ash clouds obtained from satellite infrared sounder measurements is closely related to the spectrum of the ash RI and cloud parameters. Furthermore, it supports the proposals of Reed et al. (2018) and Prata et al. (2019) that an appropriate RI model for VAC retrieval from satellites can be determined using the NBO/T (or $SiO_2$ content) of the ash samples. In addition, our results suggest that the

625 optimal RI model can be identified using only infrared sounder measurements for the VAC under certain atmospheric conditions to conduct radiative transfer calculations, provided that enough RI models have been prepared in advance.

### 5.3 Calbuco

630    In the series of Calbuco volcanic activity from 22 April 2015, IASI data for brightness temperature at 13:29–13:32 UTC on 24 April were used for our retrieval analysis. At this time, ash clouds with negative $\Delta TB_{split}$ were observed over the Atlantic Ocean near the estuary of the La Plata River at latitudes of 35–38° S and longitudes of 55–56° W (Calbuco_A: Fig. 9b), as well as over the Pacific Ocean near the west coast of Chile at 32–33° S and 73–76° W (Calbuco_B: Fig. 9e). From the MODIS colour image taken at 13:35 UTC (Fig. 9a), it appeared that the effect of MCs on the BTS was small for pixels with large

635    negative values of $\Delta TB_{split}$ in Calbuco_A. Although another VAC was confirmed around latitude 40° S in the MODIS image shown in Fig. 9a, the IASI pixels had slightly negative or positive $\Delta TB_{split}$ values, suggesting ice particles within or above the VAC layer. BTS analyses were conducted for 15 pixels with large negative $\Delta TB_{split}$ values in Calbuco_A. Small total RMS values were obtained from the PG010–PG030 RI models with the PG2019 dataset and RE040 with the RE2018 dataset, and the smallest RMS was obtained from RE040 (Fig. 5). The estimated $r_{eff}$ values were small overall, and were less than 0.2 μm

640    for most pixels when relatively mafic RI models (PG030–PG100 of PG2019 dataset) were applied. For the RE040 RI model, low $r_{eff}$ of less than 0.2 μm were obtained for most of the analysed pixels, and the smallest effective radius $r_{eff} = 0.1$ μm in our LUT was estimated for 10 of the 15 total pixels within Calbuco_A. These small $r_{eff}$ values are mainly related to the fitting of the BTS in the range of $1070 \, \text{cm}^{-1} \leq \nu \leq 1230 \, \text{cm}^{-1}$, as discussed in section 5.1 (Fig. 7). The area of pixels with large negative $\Delta TB_{split}$ in Fig. 9b is ~1500 km from Calbuco volcano, and the particle size of the VAC should be reduced due to

645    depositional segregation during transportation in the atmosphere. Although a $r_{eff} < 0.2$ μm may not be too small for the ash particles present in this area, we considered the PG020 RI model, which had the second smallest RMS after RE040 and averaged $r_{eff} \geq 0.2$ μm, to be the optimal RI model in this study. As shown in Fig. 9c, the absorption feature of $SO_2$ gas is clearly apparent in the measured BTS, and the results of BTS simulations approximately agree with the measurements. However, the RMS values between measurements and simulations were relatively large for all pixels and systematic deviation

650    from the measurements occurred even with PG020.

MODIS observed the Calbuco_B region at 15:00 UTC (Fig. 9d). We inferred the presence of an optically thin VAC in an area with little MCs, although the MODIS observation was made 1.5 hours after that of IASI. As $SO_2$ absorption features were not present in the BTS from IASI measurements, we deduced that the measured BTS patterns mainly arise from the optical properties of the VAC. In BTS simulations for 10 pixels in Calbuco_B, high-ranking RI models tended to have greater NBO/T in the PG2019 dataset compared with the results of Calbuco_A (Fig. 5); results from the RI models PG020–PG080 and RE040–

655    RE050 had small RMS values and the smallest RMS was obtained for PG050. The reason for this difference between the results of Calbuco_A and Calbuco_B has not been determined. According to the compositional analyses of Romero et al. (2016) and Deguine et al. (2020), Calbuco ash samples are of the basaltic andesite type with 55–56.3 $SiO_2$ wt. %, which is a similar or more mafic composition than Eyjafjallajökull ash samples. Our results for Calbuco_B pixels are relatively

660    consistent with the compositional analysis results, but the PG050 RI had large RMS errors for Calbuco_A pixels in our retrieval analysis. By contrast, the difference of RMS values between PG050 and PG020 is generally small in BTS simulations, as shown in Fig. 9f. Therefore, to explain the BTS based on both Calbuco_A and Calbuco_B measurements, we treated PG020 as the optimal RI model for Calbuco VAC retrieval.

665

670

675

680

685
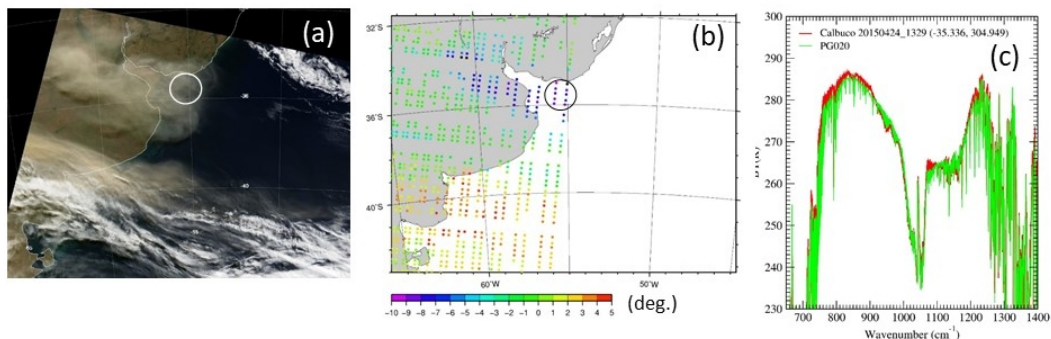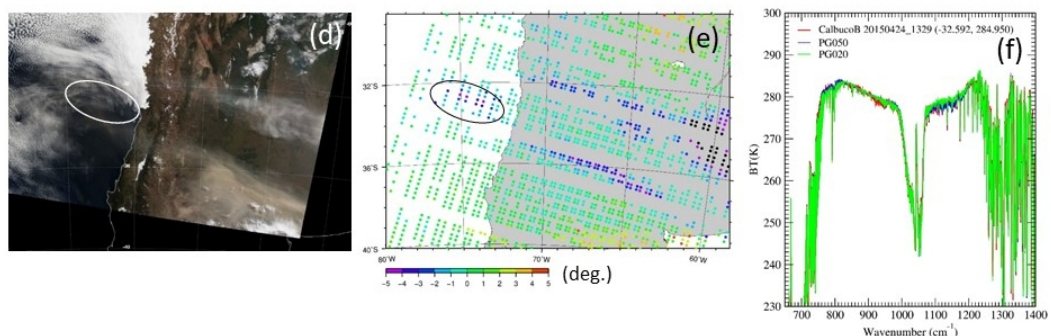
**Figure 9: Brightness temperature difference $\Delta TB_{split}$ of Calbuco ash clouds measured by IASI at 13:29 UTC on 24 Apr 2015 over**
**the Atlantic Ocean [Calbuco_A, (b)], and the measured (red) and calculated (PG020, green) BTSs for the pixel at $(lat, lon) =$**
**$(35.336°\,S, 55.051°\,W)$ (c). MODIS visible-colour image of the same region at 13:25 UTC (a). (d–f) Same as (a–c) but for ash clouds**
**over the Pacific Ocean [Calbuco_B, marked with a circle in (e)] and the measured BTS at $(lat, lon) = (32.592°\,S, 75.050°\,W)$.**
**Calculated BTSs without SO2 gas from the PG050 (blue line) and PG020 (green line) RI models are also shown. The measurement**
**time of the MODIS colour image (d) was 15:00 UTC.**

### 5.4 Kirishimayama and Nishinoshima

During the Kirishimayama eruption on 26 January 2011, ash plumes were transported in the southeast direction over the Pacific
700 Ocean, and IASI measured the VAC to the south of the Japanese main islands at 00:08 UTC on 27 January (Fig. 10b). The
MODIS image taken at 01:05 UTC (Fig. 10a) suggests that the VAC in the region of highly negative $\Delta TB_{split}$ is distributed
above the streaks of MCs, and VACs with lower MC contamination are expected in locations between the MC streaks. Due to
the 1-hour time difference between IASI and MODIS measurements, the pixels for analysis were determined using only IASI
data. Among 30 pixels of $\Delta TB_{split} < -2K$, 21 pixels were rejected under the condition of Eq. (2), suggesting that many IASI
705 pixels were contaminated with MCs. For the BTSs of the remaining nine pixels, the RI models RE080, RE020, and PG020
provided small RMS values. The results of BTS simulations for RE080 and RE020 generally agree with measured values (Fig.
10c). However, some small differences between the measured and calculated BTSs were confirmed, such as a negative bias in
the RE080 simulation around $920\ cm^{-1}$ and a positive bias in the RE020 simulation around $900-1000\ cm^{-1}$. From the
ranking plot shown in Fig. 5 for the PG2019 dataset, the Kirishimayama VAC at this time tended to fit the results of RI models
710 with smaller NBO/T values than the Eyjafjallajökull and Grímsvötn ash clouds. This result is reasonable considering the
reported SiO2 contents of the ash samples and the average local maximum of $\bar{v}_a \approx 830\ cm^{-1}$, which is a greater wavenumber

than the local maxima for Eyjafjallajökull and Grímsvötn (Table 2). However, the possibility of MC contamination of the BTSs for all VAC pixels in this area cannot be excluded. Further precise analysis of the Kirishimayama VAC, including night-time measurements with no MC contamination, is necessary. An algorithm for detecting MC contamination in the VAC using infrared channels will be essential to solving this problem.

Compared to Kirishimayama, the VACs of Nishinoshima, which were observed by IASI at 00:08 (Fig. 10e) and 23:47 UTC on 31 July 2020, were less affected by MC contamination due to the simultaneous measurements taken by the AHI onboard the geostationary satellite Himawari-8 (Fig. 10d). In BTS simulations for 18 pixels with large negative values of $\Delta TB_{split}$, the RI models RE070 with the RE2018 dataset and PG060–PG080 with the PG2019 dataset returned small RMS values and small effective radius estimates ($r_{eff} \leq 0.6$ μm) for all pixels. The smallest RMS was obtained with RE070. As shown in Fig. 10f, the calculated BTS fit well to the measured BTS, especially at wavenumbers $\nu \geq 1050$ cm$^{-1}$, but systematic errors in the range of 750 cm$^{-1} \leq \nu \leq 1000$ cm$^{-1}$ were also observed.
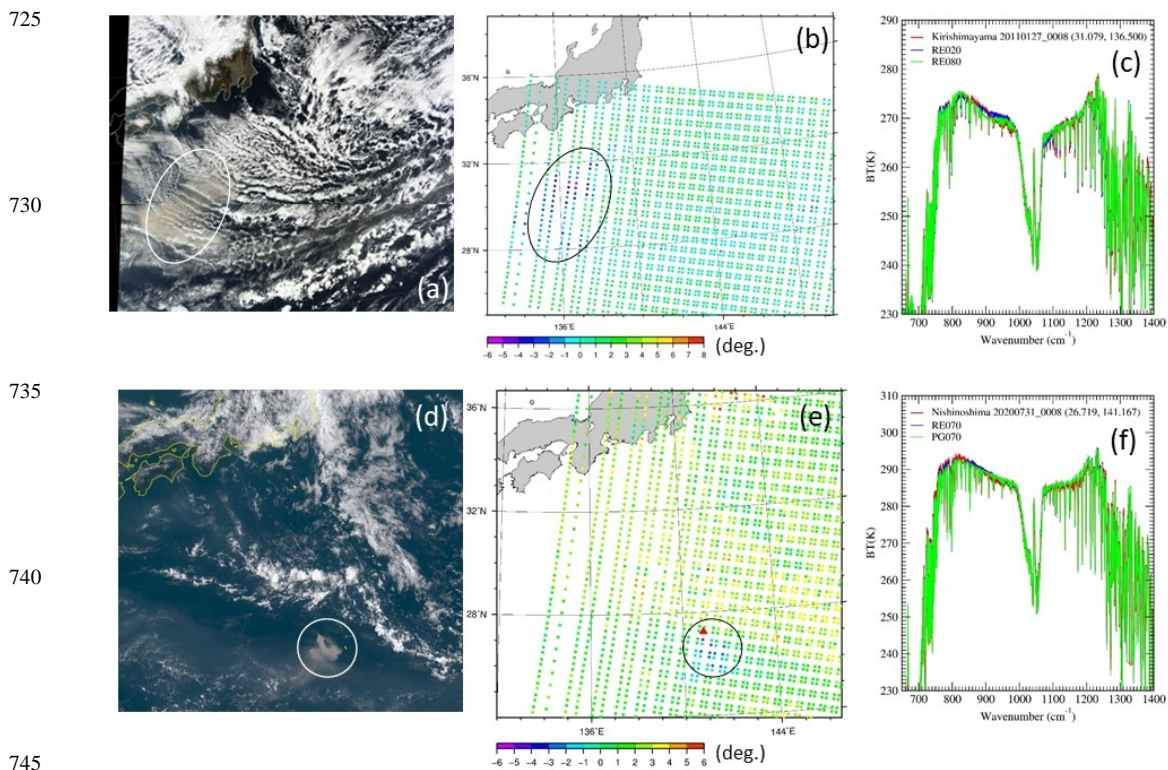
**Figure 10: (a–c) Composite MODIS image of the Kirishimayama VAC at 01:05 UTC on 27 January 2011(a), and $\Delta TB_{split}$ from IASI data at 00:08 UTC on the same day (b). Results of BTS simulations for the pixel at $(lat, lon) = (31.079°$ N, $136.500°$ E) are shown in (c), as well as the measured values. The RI models RE020 (blue) and RE080 (green) were used for the BTS simulations. For the Nishinoshima VAC on 31 July 2020, the visible true-colour image (d) is from the Himawari-8/AHI observation at 0:00–00:09 UTC, and $\Delta TB_{split}$ is from IASI at 00:05–00:08 UTC (e). (f) Measured and calculated BTSs for the pixel at $(lat, lon) = (26.719°$ N, $141.167°$ E). The RI models RE070 (blue) and PG070 (green) were used for simulations.**

755

### 5.5 Kelut

For the VAC from the Kelut eruption event on 13 February 2014, Ishimoto et al. (2016) analysed data obtained by the Atmospheric Infrared Sounder (AIRS) onboard the Earth Observing System Aqua polar-orbiting satellite and estimated that the spectral RI of the Kelut VAC was intermediate between the andesite model and the rhyolite (obsidian) model of PL1973.

760 In their analysis, a mixture of these two RI models was assumed as the a priori RI and the spectral RI in the wavenumber range of $\nu \geq 1100$ cm$^{-1}$ was omitted due to missing spectral data between 1137 and 1216 cm$^{-1}$ from the AIRS measurements. Furthermore, MC contamination was not considered for pixels with highly negative $\Delta TB_{split}$ values, although MC contamination may cause large errors in RI estimation. For the Kelut VAC at this time, Kylling (2016) reported that a mixture of ice clouds and ash clouds in an IASI pixel can explain the observed BTS from the PL1973 andesite model. In this work,

765 retrieval analyses of the Kelut VAC were repeated using IASI pixels with less MC contamination, as estimated from visible images and from the condition of Eq. (2).

In the IASI data of the Kelut VAC observed at 02:08 UTC on 14 February (Fig. 11c), all pixels with $\Delta TB_{split} < -2$K in the region of $8.0°$ S $\leq lat \leq 9.5°$ S and $106.5°$ E $\leq lon \leq 109.5°$ E were rejected under the condition of Eq. (2), and four pixels (indicated by the circle in Fig. 11c) were retained for our retrieval analysis. This result suggests that most VAC measurements

770 are affected by MC contamination, which is consistent with the conclusion of Kylling (2016) that IASI measures both ash and ice clouds in the same pixel. The area of the four retained pixels is presumed to be covered with thin ash clouds and have less MCs based on the MODIS true-colour image taken at 03:35 UTC (Fig. 11a) and the Himawari-7 visible monochromatic image taken at 02:00 UTC (Fig. 11b). The results of BTS simulations showed that the BTS of the Kelut VAC could be well simulated using relatively felsic RI models with small NBO/T values and the PG2019 dataset (Fig. 5), with PG000 and PG010 leading

775 to the smallest RMS values (Fig. 11d). Although the measured BTSs for pixels in the area of $8.0°$ S $\leq lat \leq 9.5°$ S and $106.5°$ E $\leq lon \leq 109.5°$ E are negatively biased due to MC contamination, their spectral features, such as the wavenumber of the local maximum ($\nu_a$), were similar to those shown in Fig. 11d (plots of BTSs for the Kelut VAC are also shown in Clarisse and Prata (2016)). Whether these measured BTSs can be simulated well by internal or external mixing between the andesite model of VAC and ice cloud remains unclear. In addition to internal mixing between ash and ice based on effective

780 medium theory, a simple external mixing process between individual ash and ice layers was examined through preliminary calculations, and the BTS simulations were unsuccessful. We could not conclude that Kelut ash clouds were composed of felsic ash materials based on the chemical composition (~55 SiO$_2$ wt. %) of Kelut ash samples from the same eruption (Maeno et al., 2019). However, the measured BTSs of the Kelut VACs in this eruption event can be well explained by assuming that ash particles in the Kelut VACs had a similar infrared RI feature to PG000 and PG010.

785

790
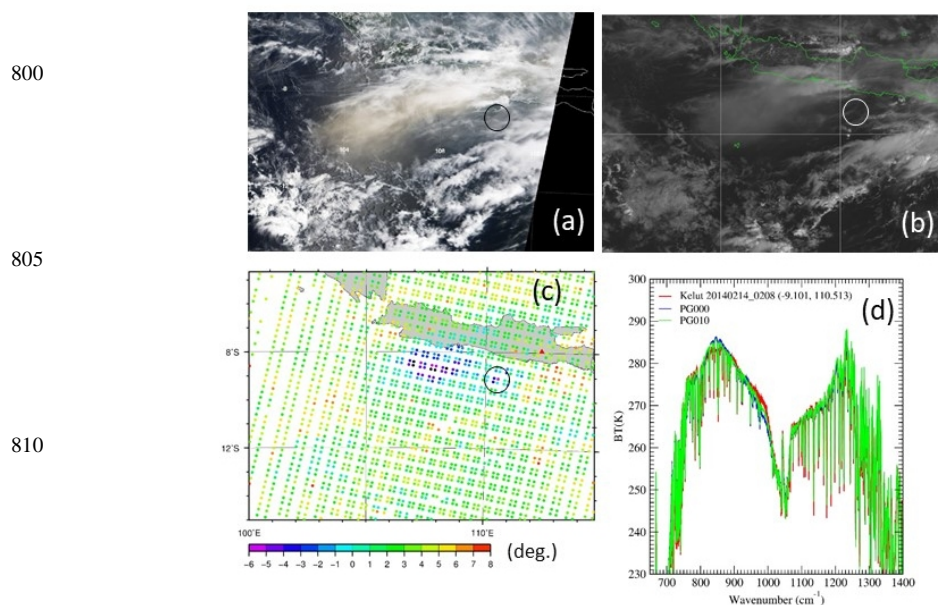
795

**Figure11: Kelut ash clouds on 14 February 2014. MODIS true-colour image taken at 03:35 UTC (a) and monochromatic Himawari-7 visible image taken at 02:00 UTC (b). $\Delta TB_{split}$ from the IASI measurement at 02:08 UTC (c) and measured and calculated BTSs for the pixel at $(lat, lon) = (9.101°\,S, 110.513°\,E)$ (d) [indicated by circles in (a–c)].**

### 5.6 Puyehue-Cordón Caulle (PCC)

From the beginning of the eruption on 4 June 2011, large amounts of volcanic ash and $SO_2$ gas were ejected from PCC, and the plumes reached an altitude of 12–13 km. Subsequently, ash clouds remained at high latitudes of the southern hemisphere for a long time (Theys et al., 2013; Klüser et al., 2013; Clarisse et al., 2013). BTS analysis was conducted for ash clouds observed over the Atlantic Ocean at 10:41–10:47 UTC and 12:29 UTC on 6 June. In the area of the IASI measurements at 10:41–10:47 UTC (Fig. 12c), MODIS observations were made at 11:05 UTC (Fig. 12b) and 12:45 UTC (Fig. 12a). From these MODIS images, ash clouds in the area with highly negative values of $\Delta TB_{split}$ based on IASI measurements were distributed above broken MCs, and BTS simulations were performed for 29 IASI pixels that met the condition of Eq. (2). In addition, ten additional IASI pixels were selected in the area of latitude 40–42° S and longitude 60–63° W from the data obtained at 12:29 UTC to avoid low-level dense MCs (circles in Fig. 12e, f). As shown in the ranking plot in Fig. 5, almost all pixels have similar spectral features, and smaller RMS values were obtained for RI models with smaller NBO/T values in the PG2019 dataset. The smallest RMS was obtained for PG000 among all RI models. In accordance with the results of BTS analysis conducted by Newman et al. (2012), felsic RI models agreed well with the compositional analysis results of ash sampled by Castro et al. (2013). Comparing BTSs from simulations and measurements, the simulation results obtained using PG000 differ significantly from the observations (Fig. 12d, g). Although the simulation results show a good fit to measurements in the wavenumber region of 820–1000 $cm^{-1}$ and at wavenumbers greater than 1130 $cm^{-1}$, a large difference in brightness temperature at wavenumbers less than 820 $cm^{-1}$ suggests an excess of relative absorption in the PG000 RI model. Moreover, the simulated BTS values were significantly larger than measurements between 1070 and 1130 $cm^{-1}$, particularly for pixels in the area

shown in Fig. 12c. In the results of VAC parameter retrieval using PG000, the effective radius $r_{eff}$ was less than 0.5 µm for

840 most pixels, and $r_{eff}$ tended to decrease as distance from PCC increased, and most of the retrieval results showed $r_{eff} \leq$ 0.3 µm for pixels around $(lat, lon) = (27°\,S, 25°\,W)$ (circle in Fig. 12c), which is 4500–4600 km from PCC. Considering a decrease in large particles due to deposition during a long transport period in the atmosphere, $r_{eff} \leq 0.3$ µm may be realistic in the case of PCC. Ash clouds from PCC eventually circled the southern hemisphere three times. Very small ash particles may increase the longevity of PCC ash clouds (Carn and Krotkov, 2016). According to the results of measurements by Cloud-

845 Aerosol Lidar with Orthogonal Polarization onboard Cloud-Aerosol Lidar and Infrared Pathfinder Satellite Observations, PCC ash clouds are mainly composed of fine-mode non-spherical ash particles with a low sulphate contribution (Vernier et al., 2013; Prata et al., 2017a). For BTSs in the range of 1070–1200 $cm^{-1}$, the RI model MP_R provides a better fit than PG000 (data not shown). This result suggests that an RI model with a stronger absorbing feature in the index $k$ around 1050 $cm^{-1}$ than that of PG000 is better for explaining the measured BTS of PCC ash clouds.

850
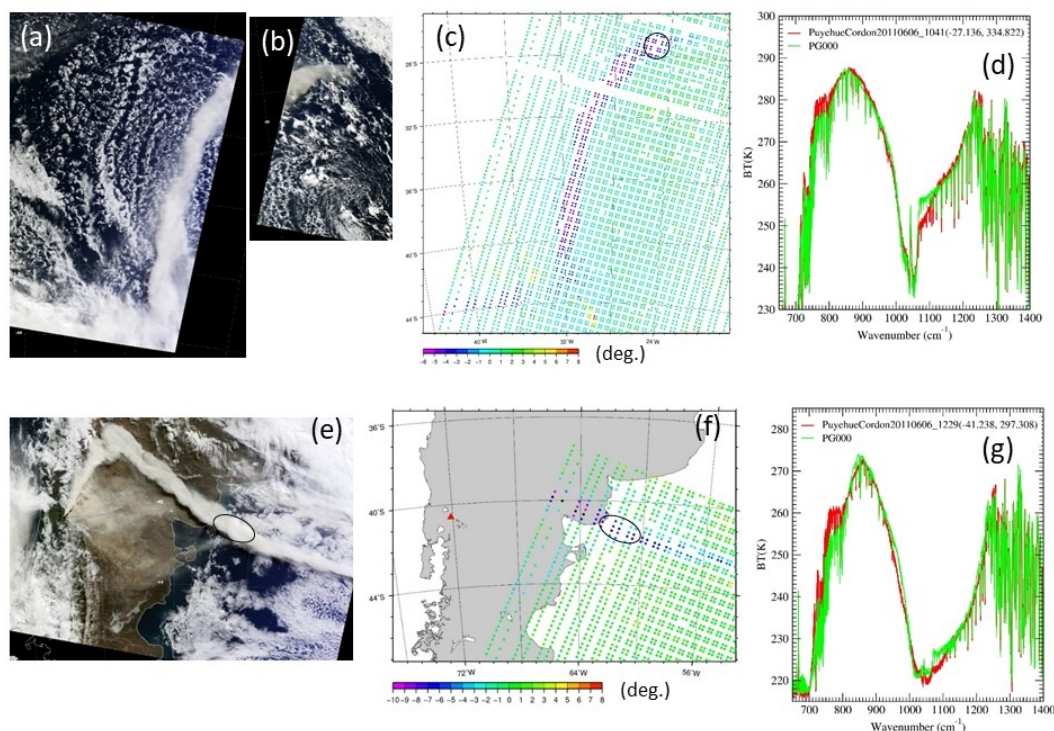
**Figure 12. (a–c) MODIS true-colour images at (a) 12:45 UTC and (b) 11:05 UTC, and (c) IASI $\Delta TB_{split}$ at 10:41–10:47 UTC for Puyehue-Cordón Caulle ash clouds on 6 June 2011. (d) Results of BTS simulation with the PG000 RI model for the pixel at $(lat, lon) = (27.136°\,S, 25.178°\,W)$. (e–g) MODIS image at (e) 14:25 UTC and (f) IASI $\Delta TB_{split}$ at 12:29 UTC. (g) Results of BTS**

875 **simulation for the pixel at $(lat, lon) = (41.238°\,S, 62.692°\,W)$.**

**5.7 Bezymianny, Zhupanovsky, Rinjani, and Sarychev Peak**

In analyses of VACs from Bezymianny, Zhupanovsky, Rinjani, and Sarychev Peak, a small number of IASI pixels could be

880 obtained due to the relatively small areas of the VACs (Bezymianny, Zhupanovsky, Rinjani), or due to distinct MC

contamination of most $\Delta TB_{split} < -2K$ pixels in MODIS visible images (Sarychev Peak). Therefore, we omit detailed discussion of these volcanic events, and simply present the results of our analyses. The dates and times of the satellite observations and retrieval parameters are listed in Tables 2 and 3, respectively. For the VAC of Sarychev Peak, one IASI pixel in an area of low MC contamination based on comparison with MODIS imagery (indicated by a circle in Fig. 13j) was used

885    for retrieval analysis. For these four volcanic events, the results of our analyses indicate good BTS fits between simulations and measurements, but whether the best-fit RI model is the optimal RI model remains unclear due to the small number of retrievals. Validation of the results using other eruption events is necessary in the future.

890

895

900

905

910

915

920
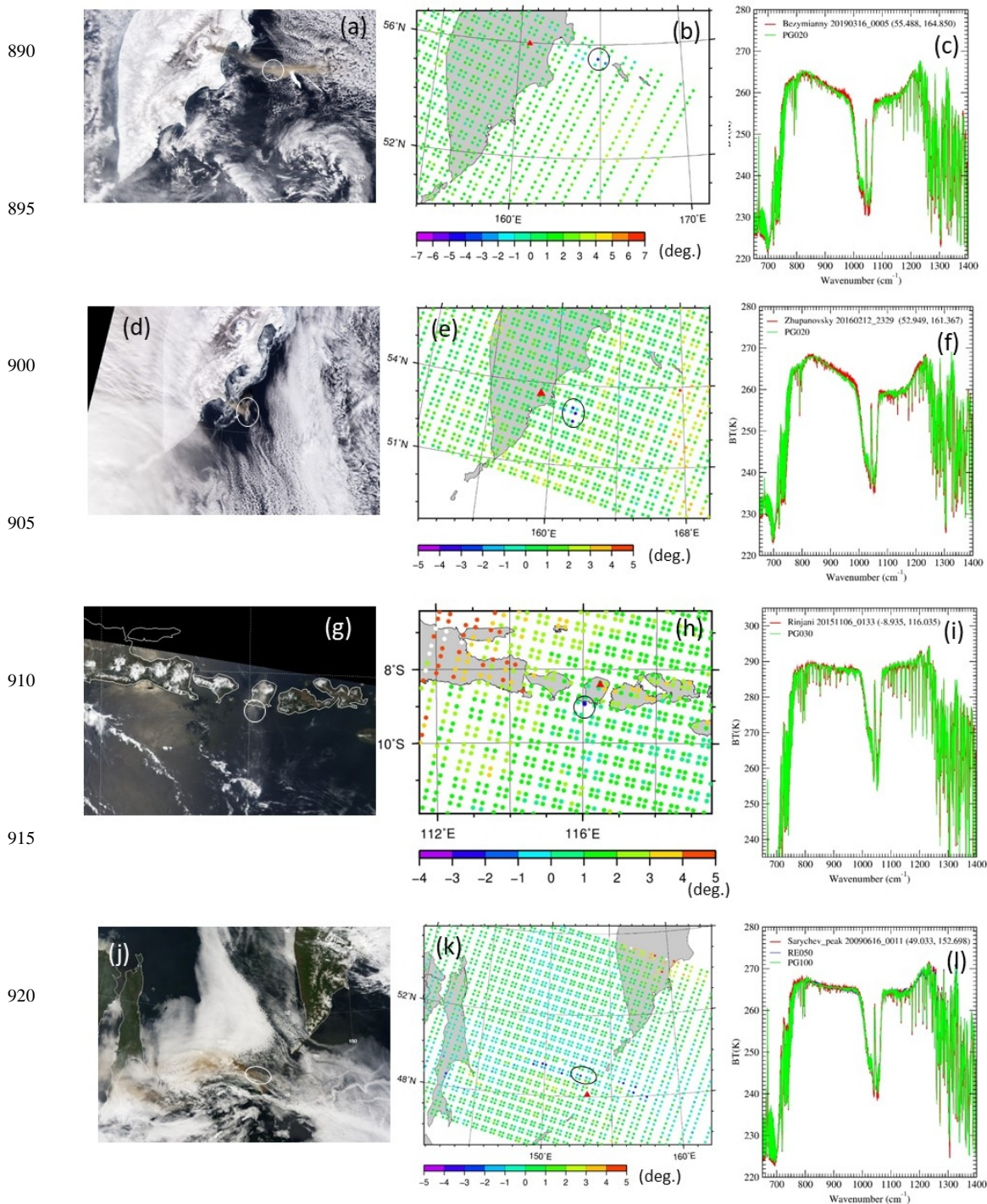
**Figure 13: Split image showing (a) the Bezymianny ash clouds observed by IASI on 16 March 2019 at 00:05 UTC and (b) the measured ash cloud BTS at** $(lat, lon) = (55.488° \text{ N}, 164.850° \text{ E})$**, along with the results of numerical simulation (green) using the**

925 **PG020 RI model (c). (a) MODIS colour image of the same area taken at 0:00 UTC on 16 March. (d–f) Same as (a–c) but for Zhupanovsky ash clouds. (e) Split image of the IASI observation on 12 Feb. 2016 at 23:29 UTC, (f) the measured ash cloud BTS at** $(lat, lon) = (53.9494° \text{ N}, 161.367° \text{ E})$ **and the results of numerical simulation (green) using the PG020 RI model. (d) MODIS colour image of the same area taken at 23:55 UTC. (g–i) Rinjani ash clouds. (g) MODIS colour image of the VAC area observed at 03:00 UTC. Split image of the IASI observation on 6 Nov. 2015 at 01:33 UTC (h), the measured ash cloud BTS at** $(lat, lon) =$

930 $(8.935° \text{ S}, 116.035° \text{ E})$**, and the results of numerical simulation using the PG030 RI model (i). Brown colour in the area of** $lon \leq$ **115° E is due to sun glint. (j–l) Sarychev Peak ash clouds. MODIS colour image of the VAC area observed at 00:50 UTC (j). Split image of the IASI observation on 16 JUN 2009 at 00:11 UTC (k), measured ash cloud BTS at** $(lat, lon) = (49.033° \text{ N}, 152.698° \text{ E})$**, and the results of numerical simulation using the RE050 RI model (blue) and PG100 RI model (green) (l). The analysis was conducted using the IASI pixels within the areas indicated with circles in (j) and (k).**

935

## 6. Summary and discussions

Using infrared brightness temperature data from IASI measurements of VACs and radiative transfer calculations, we aimed to

940 identify optimal RI models for ash particles that could reproduce the measured BTSs. We applied a total of 21 RI models to BTS simulations, including eight RI models using the RE2018 dataset, 11 RI models using the PG2019 dataset, and two additional RI models based on the andesite and rhyolite models of PL1973. For the eruption events of 11 volcanoes, 164 daytime IASI pixels containing apparent volcanic ash features ($\Delta TB_{split} \leq -2$K) with low MC contamination were selected with reference to MODIS and Himawari-8/AHI visible-colour images and an additional brightness temperature condition. The

945 BTS simulation for each pixel included retrieval of VAC parameters $(h_{top}, r_{eff}, \tau_c)$, SO$_2$ column content, and the RMS between the measured and simulated BTSs for each RI model was calculated. The results of the RI models were ranked based on the smallest RMS values for each pixel, and the optimal RI models for the target volcanoes were determined on the basis of the total RMS. Typical BTS simulation results were discussed for the ash clouds of some volcanoes. The findings obtained from these analyses are summarised below.

950 Using RI models based on new RI datasets (RE2018, PG2019), the accuracy of brightness temperature simulation for VACs in the atmospheric window region was greatly improved. In particular, RI models using the PG2019 dataset performed well, and they were selected as the optimal RI models for 10 out of 11 volcanic events. This finding suggests that the NBO/T parameterisation of Prata et al. (2019) is effective for the RI at infrared window wavelengths. Moreover, in analyses of each pixel, RI models parameterised with NBO/T often showed better BTS fits than the RI models of Reed et al. (2018) , which

955 were estimated directly from samples of specific volcanoes. This result indicates that simplified and generalised RI models created by removing small fluctuation components provide a convenient method to simulate measured BTS features.

In our BTS simulations, RI models for Eyjafjallajökull (RE030, RE040) with the RE2018 dataset and RI models parameterised using similar NBO/T values to those of Eyjafjallajökull ash samples (PG030, PG040) represented the measured BTSs of Eyjafjallajökull ash clouds with good accuracy. Such consistency was also observed for Grímsvötn ash clouds. The one-to-

960 one correlation between ash samples and ash cloud measurements based on RI for the same volcanic event indicates that the optimal RI model for ash materials can be determined from hyperspectral sounder measurements as well as NBO/T and SiO$_2$ wt. % data obtained from compositional analysis of ash samples under the condition that sufficient RI models are available in advance. Although we used the RI models of the RE2018 and PG2019 datasets, which were developed from laboratory experiments of RI and the chemical compositions of ash samples, our basic approach is to estimate the RI model from satellite

965 measurements, and the results for Eyjafjallajökull and Grímsvötn support the validity of our process.

The RI models developed from BTS simulations of IASI measurements were not always consistent with models deduced from the reported chemical compositions of ash samples. For ash clouds released from Calbuco, Kelut, Zhupanovsky, and Bezymianny, the RI models determined from IASI measurements were more felsic (or had lower NBO/T) than the rock type or $SiO_2$ wt. % of tephra samples of the corresponding volcano. Furthermore, some RI models were excluded from the optimal

970 RI models despite good BTS fitting results because the retrieved effective radii were smaller than 0.2μm. Negative values of brightness temperature difference $\Delta TB_{split}$ are greater for ash particles of smaller sizes, and therefore our analysis is biased toward ash clouds with small $r_{eff}$. In addition, the retrieved $r_{eff}$ values tended to be smaller when mafic RI models were used compared to the results of felsic RI models. This difference is due to fitting of the measured BTS in the wavenumber range of $950 \text{ cm}^{-1} \leq \nu \leq 1230 \text{ cm}^{-1}$, excluding the ozone absorption band. An effective radius of less than 0.2 μm is too small for

975 fresh ash clouds shortly after eruption, but may be realistic for ash clouds that have undergone long-distance transport in the atmosphere. Moreover, the condensation of volcanic sulphate on pure ash particles during transport might alter the inherent optical properties of the ash clouds. In particular, a retrieved $r_{eff} \leq 0.2$ μm may be reasonable for ash clouds measured far from the volcano, such as those from Calbuco and Puyehue-Cordón Caulle observed over the Atlantic Ocean.

We used a modified version of the andesite model (MP_A), in which a weak absorption feature in the range of 700–850 cm$^{-1}$

980 was added. Although the modified RI model showed better fitting results than the original andesite model of PL1973 in our BTS analysis, it was not selected as the best RI model for all IASI pixels in this study. This result indicates that substantial improvement in satellite retrieval results for VACs can be expected from replacing the conventional andesite model with a proper RI model based on the RE2018 and PG2019 datasets. We explored the reproducibility of measured BTSs over the entire wavenumber range of 650–1400 cm$^{-1}$, including bands for $CO_2$, water vapour, ozone, and $SO_2$, and noted that the estimated

985 RI models may not produce good results for VAC parameters in retrievals from multi-channel satellite imagers using certain infrared wavelength channels.

In this study, we used MODIS and Himawari-8 daytime visible images for rough estimation of MC contamination in IASI measurement areas. For that reason, the number of IASI pixels available for analysis was significantly reduced, and statistical evaluation of the retrieval results for some volcanic events was difficult. To achieve a sufficient number of analyses, thorough

990 evaluation of MC contamination of night-time VAC data from infrared sounder measurements is necessary, and methods for such evaluation should be explored in future research. In recent years, plans for mounting infrared sounders on geostationary satellites have been undertaken. High-frequency observations of distinct volcanic plumes increase the number of BTS data available, and precise retrieval is expected with further improvements in VAC analysis to combine infrared sounder and high-resolution imager measurements.

995 We tested 21 RI models in this article, and conspicuous discrepancies in measured and calculated BTSs at specific wavenumber ranges were confirmed in all RI models for some volcanic events. This finding suggests that the number of RI models is still insufficient for simulating all BTS patterns of VACs for various types of volcanoes. Recently, another RI dataset based on laboratory analysis of ash samples of six volcanoes was published by Deguine et al. (2020), and the data are available from the journal website. We conducted the same BTS analysis for VAC pixels for the Calbuco, Eyjafjallajökull, Grímsvötn, and

1000 Puyehue-Cordón Caulle events using the corresponding RI models. However, the results of these BTS simulations did not change the ranking or selection of optimal RI models in this paper. Compared to the RE2018 and PG2019 datasets, peaks of the absorption index $k$ in the RI models of Deguine et al. (2020) are shifted toward longer wavelengths, which appears to increase the RMS between measurements and our simulation results. Deguine et al. (2020) notes that this difference in the absorption index is related to the differing assumed shape of ash particles in laboratory analysis of ash samples, as Deguine et

1005 al. (2020) considered a spherical shape and applied Mie theory to the optical properties of sampled ash particles, while Reed et al. (2018) used the results of the Rayleigh CDE. If the spectral features of the resultant RI model are affected by the assumed ash shape, realistic shape models for ash particles may lead to novel RI models that agree well with the BTSs of ash clouds

observed with satellite infrared sounders. We hope that the RI models of Deguine et al. (2020) can be modified to consider the non-spherical nature of volcanic ash particles in future research.

1010

## References

Bessho, K., Date, K., Hayashi, M., Ikeda, A., Imai, T., Inoue, H., Kumagai, Y., Miyakawa, T., Murata, H., Ohno, T., Okuyama, A., Oyama, R., Sasaki, Y., Shimazu, Y., Shimoji, K., Sumida, Y., Suzuki, M., Taniguchi, H., Tsuchiyama, H., Uesawa, D., Yokota, H. and Yoshida, R.: An Introduction to Himawari-8/9 -Japan's New-Generation Geostationary

1015   Meteorological Satellites, J. Meteorol. Soc. Japan. Ser. II, 94(2), 151–183, doi:10.2151/jmsj.2016-009, 2016.

Buehler, S. A., John, V. O., Kottayil, A., Milz, M. and Eriksson, P.: Efficient radiative transfer simulations for a broadband infrared radiometer—Combining a weighted mean of representative frequencies approach with frequency selection by simulated annealing, J. Quant. Spectrosc. Radiat. Transf., 111(4), 602–615, doi:10.1016/j.jqsrt.2009.10.018, 2010.

Carn, S. A. and Krotkov, N. A.: Ultraviolet Satellite Measurements of Volcanic Ash, in Volcanic Ash, edited by S. Mackie,

1020   K. Cashman, H. Ricketts, A. Rust, and M. Watson, pp. 217–231, Elsevier., 2016.

Cashman, K. and Rust, A.: Volcanic Ash: Generation and Spatial Variations, in Volcanic Ash, edited by S. Mackie, K. Cashman, H. Ricketts, A. Rust, and M. Watson, pp. 5–22, Elsevier., 2016.

Castro, J. M., Schipper, C. I., Mueller, S. P., Militzer, A. S., Amigo, A., Parejas, C. S. and Jacob, D.: Storage and eruption of near-liquidus rhyolite magma at Cordón Caulle, Chile, Bull. Volcanol., 75(4), 702, doi:10.1007/s00445-013-0702-9,

1025   2013.

Clarisse, L. and Prata, F.: Infrared Sounding of Volcanic Ash, in Volcanic Ash, edited by S. Mackie, K. Cashman, H. Ricketts, A. Rust, and M. Watson, pp. 189–215, Elsevier., 2016.

Clarisse, L., Hurtmans, D., Prata, A. J., Karagulian, F., Clerbaux, C., De Mazière, M. and Coheur, P.-F.: Retrieving radius, concentration, optical depth, and mass of different types of aerosols from high-resolution infrared nadir spectra, Appl.

1030   Opt., 49(19), 3713, doi:10.1364/AO.49.003713, 2010.

Clarisse, L., Coheur, P.-F., Prata, F., Hadji-Lazaro, J., Hurtmans, D. and Clerbaux, C.: A unified approach to infrared aerosol remote sensing and type specification, Atmos. Chem. Phys., 13(4), 2195–2221, doi:10.5194/acp-13-2195-2013, 2013.

Deguine, A., Petitprez, D., Clarisse, L., Guðmundsson, S., Outes, V., Villarosa, G. and Herbin, H.: Complex refractive index of volcanic ash aerosol in the infrared, visible, and ultraviolet, Appl. Opt., 59(4), 884, doi:10.1364/AO.59.000884, 2020.

1035   Francis, P. N., Cooke, M. C. and Saunders, R. W.: Retrieval of physical properties of volcanic ash using Meteosat: A case study from the 2010 Eyjafjallajökull eruption, J. Geophys. Res. Atmos., 117(D20), 1–14, doi:10.1029/2011JD016788, 2012.

Gangale, G., Prata, A. J. and Clarisse, L.: The infrared spectral signature of volcanic ash determined from high-spectral resolution satellite measurements, Remote Sens. Environ., 114(2), 414–425, doi:10.1016/j.rse.2009.09.007, 2010.

1040   Hansen, J. E. and Travis, L. D.: Light scattering in planetary atmospheres, Space Sci. Rev., 16(4), 527–610, doi:10.1007/BF00168069, 1974.

Harvey, N. J., Dacre, H. F., Webster, H. N., Taylor, I. A., Khanal, S., Grainger, R. G. and Cooke, M. C.: The Impact of Ensemble Meteorology on Inverse Modeling Estimates of Volcano Emissions and Ash Dispersion Forecasts: Grímsvötn 2011, Atmosphere (Basel)., 11(10), 1022, doi:10.3390/atmos11101022, 2020.

1045   Holl, G., Buehler, S. A., Mendrok, J. and Kottayil, A.: Optimised frequency grids for infrared radiative transfer simulations in cloudy conditions, J. Quant. Spectrosc. Radiat. Transf., 113(16), 2124–2134, doi:10.1016/j.jqsrt.2012.05.022, 2012.

Ishimoto, H., Masuda, K., Fukui, K., Shimbori, T., Inazawa, T., Tuchiyama, H., Ishii, K. and Sakurai, T.: Estimation of the refractive index of volcanic ash from satellite infrared sounder data, Remote Sens. Environ., 174, 165–180, doi:10.1016/j.rse.2015.12.009, 2016.

1050 Klüser, L., Erbertseder, T. and Meyer-Arnek, J.: Observation of volcanic ash from Puyehue–Cordón Caulle with IASI, Atmos. Meas. Tech., 6(1), 35–46, doi:10.5194/amt-6-35-2013, 2013.

Kylling, A.: Ash and ice clouds during the Mt Kelud February 2014 eruption as interpreted from IASI and AVHRR/3 observations, Atmos. Meas. Tech., 9(5), 2103–2117, doi:10.5194/amt-9-2103-2016, 2016.

Kylling, A., Kristiansen, N., Stohl, A., Buras-Schnell, R., Emde, C. and Gasteiger, J.: A model sensitivity study of the

1055 impact of clouds on satellite detection and retrieval of volcanic ash, Atmos. Meas. Tech., 8(5), 1935–1949, doi:10.5194/amt-8-1935-2015, 2015.

Mackie, S. and Watson, M.: Probabilistic detection of volcanic ash using a Bayesian approach, J. Geophys. Res. Atmos., 119(5), 2409–2428, doi:10.1002/2013JD021077, 2014.

Mackie, S., Cashman, K., Ricketts, H., Rust, A. and Watson, M.: Introduction, in Volcanic Ash, edited by S. Mackie, K.

1060 Cashman, H. Ricketts, A. Rust, and M. Watson, pp. 1–3, Elsevier., 2016.

Maeno, F., Nakada, S., Yoshimoto, M., Shimano, T., Hokanishi, N., Zaennudin, A. and Iguchi, M.: A sequence of a plinian eruption preceded by dome destruction at Kelud volcano, Indonesia, on February 13, 2014, revealed from tephra fallout and pyroclastic density current deposits, J. Volcanol. Geotherm. Res., 382, 24–41, doi:10.1016/j.jvolgeores.2017.03.002, 2019.

1065 Mishchenko, M. I., Travis, L. and Lacis, A. a: Scattering, Absorption, and Emission of Light by Small Particles, Cambridge, pp445, 2002.

Moxnes, E. D., Kristiansen, N. I., Stohl, A., Clarisse, L., Durant, A., Weber, K. and Vogel, A.: Separation of ash and sulfur dioxide during the 2011 Grímsvötn eruption, J. Geophys. Res. Atmos., 119(12), 7477–7501, doi:10.1002/2013JD021129, 2014.

1070 Newman, S. M., Clarisse, L., Hurtmans, D., Marenco, F., Johnson, B., Turnbull, K., Havemann, S., Baran, A. J., O'Sullivan, D. and Haywood, J.: A case study of observations of volcanic ash from the Eyjafjallajökull eruption: 2. Airborne and satellite radiative measurements, J. Geophys. Res. Atmos., 117(D20), 1–19, doi:10.1029/2011JD016780, 2012.

Pavolonis, M. J., Heidinger, A. K. and Sieglaff, J.: Automated retrievals of volcanic ash and dust cloud properties from upwelling infrared measurements, J. Geophys. Res. Atmos., 118(3), 1436–1458, doi:10.1002/jgrd.50173, 2013.

1075 Pavolonis, M. J., Sieglaff, J. and Cintineo, J.: Spectrally Enhanced Cloud Objects—A generalized framework for automated detection of volcanic ash and dust clouds using passive satellite measurements: 1. Multispectral analysis, J. Geophys. Res. Atmos., 120(15), 7813–7841, doi:10.1002/2014JD022968, 2015a.

Pavolonis, M. J., Sieglaff, J. and Cintineo, J.: Spectrally Enhanced Cloud Objects—A generalized framework for automated detection of volcanic ash and dust clouds using passive satellite measurements: 2. Cloud object analysis and global

1080 application, J. Geophys. Res. Atmos., 120(15), 7842–7870, doi:10.1002/2014JD022969, 2015b.

Plechova, A. A., Portnyagin, M. V. and Bazanova, L. I.: The origin and evolution of the parental magmas of frontal volcanoes in Kamchatka: Evidence from magmatic inclusions in olivine from Zhupanovsky volcano, Geochemistry Int., 49(8), 743–767, doi:10.1134/S0016702911080064, 2011.

Pollack, J. B., Toon, O. B. and Khare, B. N.: Optical properties of some terrestrial rocks and glasses, Icarus, 19(3), 372–389,

1085 doi:10.1016/0019-1035(73)90115-2, 1973.

Prata, A. J.: Infrared radiative transfer calculations for volcanic ash clouds, Geophys. Res. Lett., 16(11), 1293–1296, doi:10.1029/GL016i011p01293, 1989.

Prata, A. J. and Grant, I. F.: Retrieval of microphysical and morphological properties of volcanic ash plumes from satellite data: Application to Mt Ruapehu, New Zealand, Q. J. R. Meteorol. Soc., 127(576), 2153–2179, doi:10.1002/qj.49712757615, 2001.

Prata, A. T., Young, S. A., Siems, S. T. and Manton, M. J.: Lidar ratios of stratospheric volcanic ash and sulfate aerosols retrieved from CALIOP measurements, Atmos. Chem. Phys., 17(13), 8599–8618, doi:10.5194/acp-17-8599-2017, 2017a.

Prata, F. and Lynch, M.: Passive Earth Observations of Volcanic Clouds in the Atmosphere, Atmosphere (Basel)., 10(4), 199, doi:10.3390/atmos10040199, 2019.

Prata, F., Woodhouse, M., Huppert, H. E., Prata, A., Thordarson, T. and Carn, S.: Atmospheric processes affecting the separation of volcanic ash and SO2 in volcanic eruptions: Inferences from the May 2011 Grímsvötn eruption, Atmos. Chem. Phys., 17(17), 10709–10732, doi:10.5194/acp-17-10709-2017, 2017b.

Prata, G. S., Ventress, L. J., Carboni, E., Mather, T. A., Grainger, R. G. and Pyle, D. M.: A New Parameterization of Volcanic Ash Complex Refractive Index Based on NBO/T and SiO 2 Content, J. Geophys. Res. Atmos., 124(3), 1779–1797, doi:10.1029/2018JD028679, 2019.

Reed, B. E., Peters, D. M., McPheat, R., Smith, A. J. A. and Grainger, R. G.: Mass extinction spectra and size distribution measurements of quartz and amorphous silica aerosol at 0.33–19 µm compared to modelled extinction using Mie, CDE, and T-matrix theories, J. Quant. Spectrosc. Radiat. Transf., 199, 52–65, doi:10.1016/j.jqsrt.2017.05.011, 2017.

Reed, B. E., Peters, D. M., McPheat, R. and Grainger, R. G.: The Complex Refractive Index of Volcanic Ash Aerosol Retrieved From Spectral Mass Extinction, J. Geophys. Res. Atmos., 123(2), 1339–1350, doi:10.1002/2017JD027362, 2018.

Romero, J. E., Morgavi, D., Arzilli, F., Daga, R., Caselli, A., Reckziegel, F., Viramonte, J., Díaz-Alvarado, J., Polacci, M., Burton, M. and Perugini, D.: Eruption dynamics of the 22–23 April 2015 Calbuco Volcano (Southern Chile): Analyses of tephra fall deposits, J. Volcanol. Geotherm. Res., 317(April 2015), 15–29, doi:10.1016/j.jvolgeores.2016.02.027, 2016.

Rybin, A., Chibisova, M., Webley, P., Steensen, T., Izbekov, P., Neal, C. and Realmuto, V.: Satellite and ground observations of the June 2009 eruption of Sarychev Peak volcano, Matua Island, Central Kuriles, Bull. Volcanol., 73(9), 1377–1392, doi:10.1007/s00445-011-0481-0, 2011.

Sano, T., Shirao, M., Tani, K., Tsutsumi, Y., Kiyokawa, S. and Fujii, T.: Progressive enrichment of arc magmas caused by the subduction of seamounts under Nishinoshima volcano, Izu–Bonin Arc, Japan, J. Volcanol. Geotherm. Res., 319, 52–65, doi:10.1016/j.jvolgeores.2016.03.004, 2016.

Theys, N., Campion, R., Clarisse, L., Brenot, H., van Gent, J., Dils, B., Corradini, S., Merucci, L., Coheur, P.-F., Van Roozendael, M., Hurtmans, D., Clerbaux, C., Tait, S. and Ferrucci, F.: Volcanic SO2 fluxes derived from satellite data: a survey using OMI, GOME-2, IASI and MODIS, Atmos. Chem. Phys., 13(12), 5945–5968, doi:10.5194/acp-13-5945-2013, 2013.

Turnbull, K., Johnson, B., Marenco, F., Haywood, J., Minikin, A., Weinzierl, B., Schlager, H., Schumann, U., Leadbetter, S. and Woolley, A.: A case study of observations of volcanic ash from the Eyjafjallajökull eruption: 1. In situ airborne observations, J. Geophys. Res. Atmos., 117(D20), 1–19, doi:10.1029/2011JD016688, 2012.

Turner, S. J., Izbekov, P. and Langmuir, C.: The magma plumbing system of Bezymianny Volcano: Insights from a 54year time series of trace element whole-rock geochemistry and amphibole compositions, J. Volcanol. Geotherm. Res., 263, 108–121, doi:10.1016/j.jvolgeores.2012.12.014, 2013.

Ventress, L. J., McGarragh, G., Carboni, E., Smith, A. J. and Grainger, R. G.: Retrieval of ash properties from IASI measurements, Atmos. Meas. Tech., 9(11), 5407–5422, doi:10.5194/amt-9-5407-2016, 2016.

Vernier, J.-P., Fairlie, T. D., Murray, J. J., Tupper, A., Trepte, C., Winker, D., Pelon, J., Garnier, A., Jumelet, J., Pavolonis,

1130   M., Omar, A. H. and Powell, K. A.: An Advanced System to Monitor the 3D Structure of Diffuse Volcanic Ash Clouds, J. Appl. Meteorol. Climatol., 52(9), 2125–2138, doi:10.1175/JAMC-D-12-0279.1, 2013.

Wen, S. and Rose, W. I.: Retrieval of sizes and total masses of particles in volcanic clouds using AVHRR bands 4 and 5, J. Geophys. Res., 99(D3), 5421, doi:10.1029/93JD03340, 1994.